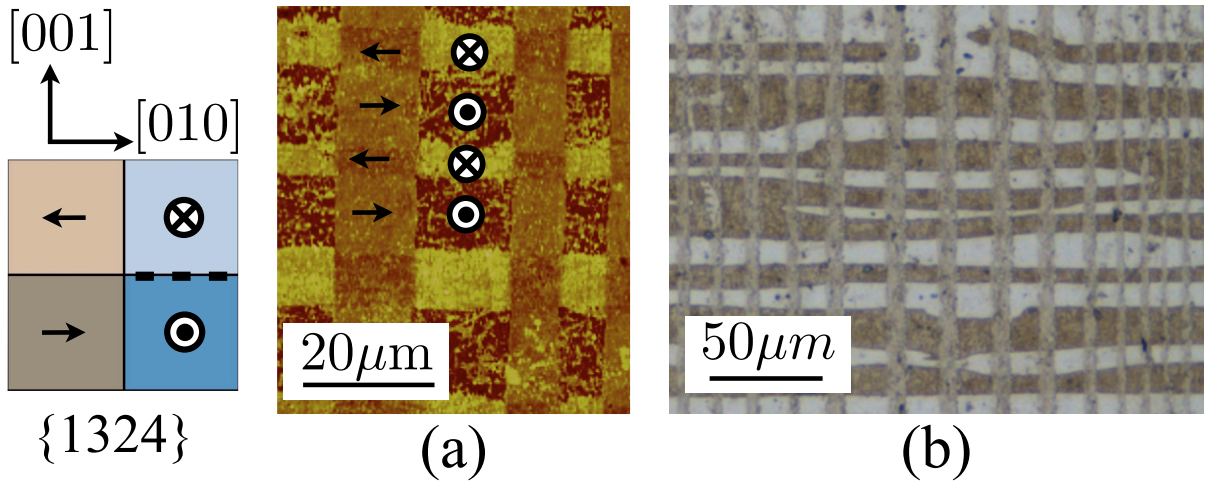

Figure 3.13: Images generated by (a) AFM and (b) optical microscopy, showing the $\{1324\}$ rank-2 laminate domain patterns.

scan rate of 1 Hz, revealing a topographic contrast of about 100 nm caused by etching. Square checks appear in patterns $\{1221\}$, $\{1324\}$ and $\{1342\}$, but here, alignment of the checks to the crystallographic axes eliminates $\{1342\}$ and makes $\{1221\}$ unlikely. The difference in etching depth between the in-plane and out-of-plane domains confirms this as pattern $\{1324\}$. It is interesting to note that the two sub-laminates (13 and 24) are separated by a $180°$ domain wall that alternates between fixed orientation and flexible orientation as it crosses the pattern, resulting in curved domain walls between the crystal variants polarized in the out-of-plane direction. Thus, the $\{1324\}$ structure can form a watermark pattern intersected by straight $90°$ domain walls as shown in figure 3.13(b), which was produced by viewing an etched $BaTiO_3$ crystal using an Alicona InfiniteFocus microscope. Similar domain configurations have been reported in previous work [101, 105].

The $\{1342\}$ pattern exhibits an array of polarization vortices, a structure that has been predicted using diffuse interface models [14, 56]. However, the pattern has not been widely observed, perhaps due to the strong disclinations present, which make this a relatively high energy state. The AFM image of etched barium titanate shown in figure 3.14 was generated using the same method as figure 3.13(a) on a different sample of barium titanate. This appears to reveal the $\{1342\}$ domain pattern, containing $90°$ domain walls in a checkerboard pattern

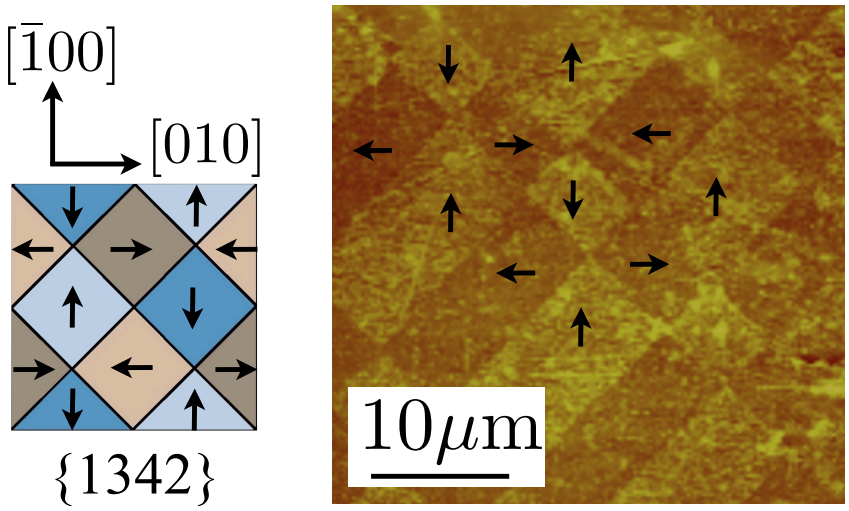

Figure 3.14: An image generated by AFM showing the $\{1342\}$ rank-2 laminate domain patterns.

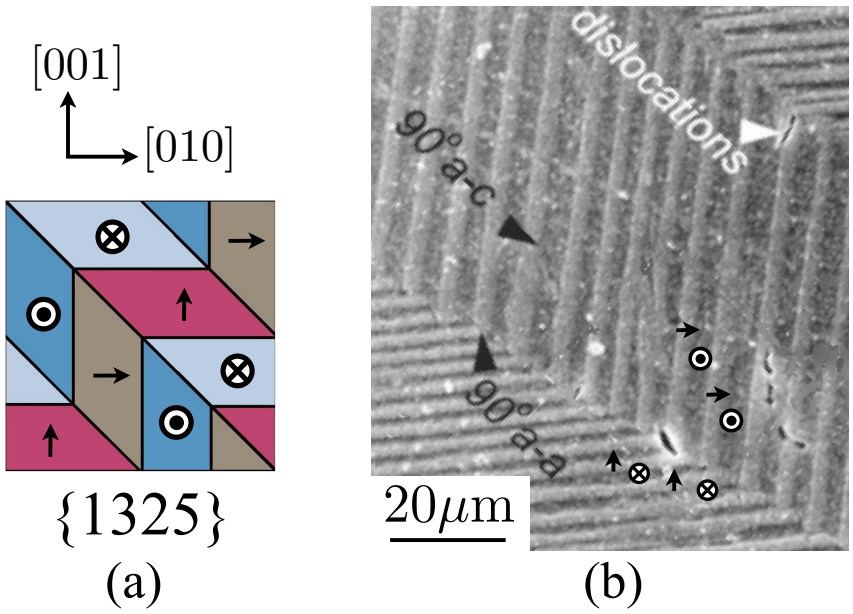

Figure 3.15: An image generated by SEM showing the $\{1325\}$ rank-2 laminate domain patterns. (modified from Cheng *et al.* [96])

oriented at 45° to the crystallographic axes. Relatively low contrast between the domains was achieved, as expected for the etching of in-plane domains.

Patterns in the $\{1325\}$ family were not found in our sample, but they have been widely observed and discussed [1, 2, 24, 93, 96, 98, 106, 107]. All the domain walls, including the 180° walls, in this pattern have orientations fixed by the requirements of compatibility. Figure 3.15(b)

Table 3.10: The 51 distinct topologies of a rank-2 laminate made of polar rhombohedral crystal variants, showing the subset of exactly compatible rank-2 laminates.

Not exactly compatible	Rank < 2, exactly compatible	Rank = 2, exactly compatible
1123 1223	1111	1112
1124 1224	1113	1213
1134 1315	1114	1214
1135 1316	1122	1221
1136 1332	1133	1234
1145 1335	1144	1243
1235 1336	1212	1314
1236 1346	1313	1324
1246 1368	1331	1325
1326 1415	1414	1342(1432)
1345 1436	1441	1357
1358 1445		1423
1467		1426
		1458

shows a SEM image of domain pattern $\{1325\}$, done by Cheng *et al.* [96]. The image has been modified and rotated accordingly for comparison. Domain patterns of $\{1213\}$ and $\{1314\}$ were also not found in our sample, but have been discussed in the literature [102].

In order to illustrate the applicability of the methods described, rank-2 laminates in the polar rhombohedral crystal system were classified by the same method. There are eight crystal variants in this crystal system; number them $1 \ldots 8$ with polarization directions and strain states as shown in equation (3.7). The 8^4 permutations of the rank-2 tree reduce using the $m3m$ symmetries to 51 distinct topologies of which only 14 are distinct exactly compatible patterns not equivalent to a lower rank structure, as listed in table 3.10. The corresponding schematic domain patterns are shown in figure 3.16. Patterns $\{1342\}$ and $\{1432\}$ have identical topology, arising from a coincidence of domain wall orientations $\mathbf{n}_2 \equiv \mathbf{n}_3$ in both patterns. Some of the patterns in table 3.10 have been found by other methods; for example a rhombohedral $\{1458\}$ laminate was predicted using phase-field methodology by Shu *et al.* [22] as was shown in figure 3.7(d). The current method provides a rapid and complete identification of minimum

energy laminates. The method is readily extended to higher rank laminates, though the number of patterns becomes large and laminates of rank greater than 2 are less commonly observed in ferroelectric crystals. Application to non-polar systems such as shape memory alloys is also possible and can be an interesting further extension.

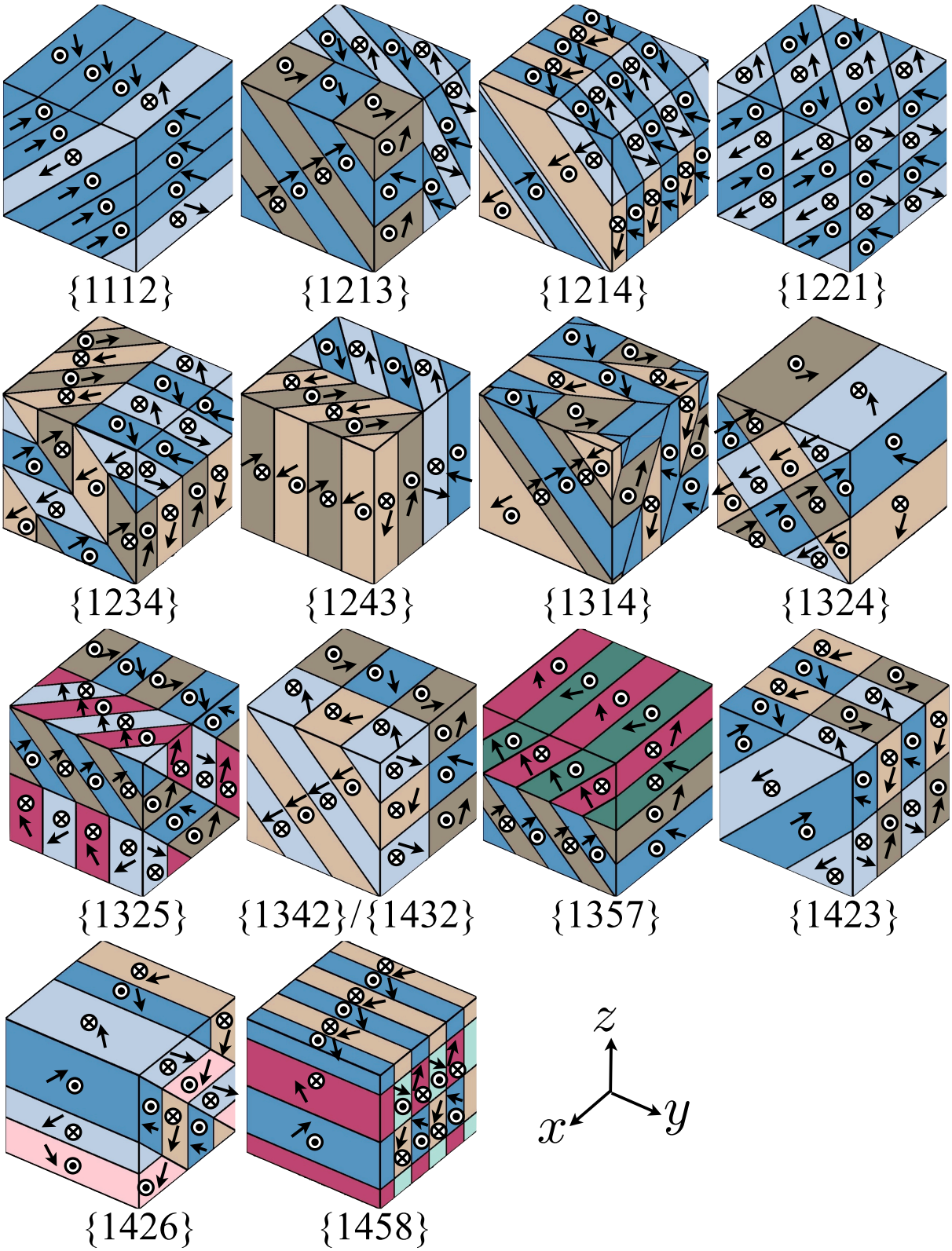

Figure 3.16: The 14 exactly compatible, periodic, rank-2 laminate domain patterns in the rhombohedral crystal system. Patterns $\{1342\}$ and $\{1432\}$ have identical topology, arising from a coincidence of domain wall orientations $\mathbf{n}_2 \equiv \mathbf{n}_3$ in both patterns.

4

Application to film devices

4.1 Exact compatibility conditions for ferroelectric films

In ferroelectric thin films, the crystal is grown on a substrate, so epitaxial growth can determine crystallographical orientation. This means a strong interaction between the film and its substrate. The substrate produces a constrained condition such that the stable domain structure depends not only on domain compatibility but also on the mismatch between film and substrate. Substrate constraint can dramatically change the properties of the film, such as Curie temperature, and the volume fractions of the crystal variants [73]. Thus, it is of interest to study domain structures in ferroelectric films under different substrate conditions and with different crystallographic orientations. In sufficiently thin films, only the in-plane compatibility conditions are required [75] because a low energy elastic accommodation to out-of-plane incompatibilities is possible. However, in this study, thicker films are considered in which the out-of-plane compatibility condition is still satisfied by low energy microstructures. This is representative of films where the domain wall spacing is of similar magnitude to the film thickness.

Consider a ferroelectric film in a low energy, compatible state, with average residual strain $\boldsymbol{\epsilon}^r$ and remanent polarization $\mathbf{P}$. It is possible to determine the total volume fraction $f_{(k)}$ of the kth crystal variant by solving equations (2.12)–(2.14) as mentioned in section 2.3.1. With the

volume fractions known, we can always construct Li-Liu type laminate structures which are compatible on average [26]. However, for certain states of macroscopic strain and polarization, it is possible to construct a laminate in ferroelectric films which satisfies the compatibility equations across every junction of the domains. To achieve this, exact compatibility must be satisfied: **(i) the condition of volume fraction ratio equivalence**; **(ii) the condition of domain wall orientation** and **(iii) the condition of compatibility between every pair of adjacent domains**, as mentioned in section 2.3.3. However, for periodic domain structures in a constrained film which is perfectly bonded to a rigid substrate, further conditions arise:

(iv) The condition that domain walls may not be parallel to the substrate. Since the film thickness is generally much smaller than its other dimensions, and we consider a periodic structure, any domain wall parallel to the substrate surface would imply multiple divisions of the film thickness into separate domains. We shall assume that the film is sufficiently thin to prohibit such division. Let the surface normal of the film be $[001]$ in global coordinates. Then, in terms of the tree diagram, $\mathbf{n}_i \nparallel [001]$ for all nodes i ($i = 1 \dots 2^R - 1$).

(v) The condition of imposed macroscopic in-plane strain. We consider a film perfectly bonded to a thick substrate, such that the average in-plane strain components of the film (ϵ^r_{11}, ϵ^r_{22}, and ϵ^r_{12}) are imposed by the substrate. These components of the average, macroscopic strain of the film must remain constant unless the substrate changes its strain state, for example by thermal expansion. Moreover, it follows from the isochoric nature of remanent straining (all crystal variants have equal unit cell volume) that $\epsilon^r_{33} = -\epsilon^r_{11} - \epsilon^r_{22}$. As in chapters 2 and 3 it is assumed that the ferroelectric crystal adapts to the imposed state of strain through remanent strain only, with no elastic straining. Then, since the in-plane strain components ($\epsilon^r_{11}, \epsilon^r_{22}$) are imposed by the substrate, this fixes the state of the average out-of-plane strain component ϵ^r_{33}.

It is worth noting that here we consider films with complete upper and lower electrodes, and thus neglect the effects of external electric field, substrate-related electrostatic interaction

and the formation of closure domains. Using the conditions (i)–(v), it is possible to identify the low-energy periodic laminate configurations of a ferroelectric film corresponding to given states of macroscopic polarization.

4.2 Method

Now, the conditions described in section 4.1 are used to find minimum rank compatible domain arrangements in ferroelectric films. We concentrate our search on laminates of the minimum possible rank, noting that low-rank structures contain fewer domain walls and so are energetically favoured, while in high-rank structures, the likelihood of satisfying all of the conditions for exact compatibility is reduced. Similar to the procedure used for bulk materials in section 3.2, an iteration procedure is used to check all of the possible arrangements until a configuration satisfying the exact compatibility conditions for films, (i)–(v), is found. Note that here the focus is on searching minimum rank exactly compatible (EC) laminates in ferroelectric films only, and structures with average compatibility (COA) and disclination-free (DF) compatibility are not reported in this chapter. The corresponding flow chart illustrating the overall iteration process is shown in figure 4.1.

The starting point for the iterative procedure is a given state of average strain $\boldsymbol{\epsilon}^r$ and polarization $\mathbf{P}$. Some components of the remanent strain tensor are imposed by the state of substrate strain, according to condition (v). The remaining components may be chosen arbitrarily, for example to achieve a desired poling state. Then, $\boldsymbol{\epsilon}^r$ and $\mathbf{P}$ along with the microscopic strain $\boldsymbol{\epsilon}_{(k)}$ and polarization $\mathbf{p}_{(k)}$ of each crystal variant are substituted into equations (2.12)–(2.14) to obtain a set of n non-zero volume fractions $f_{(k)}$ ($k = 1 \ldots n$) of each variant. If these cannot satisfy $1 \geq f_{(k)} \geq 0$, then there is no possible laminate structure for the given macroscopic state. In practice, this would correspond to a stressed configuration. Here, the focus is on those cases where a laminate structure can achieve the imposed strain and polarization state.

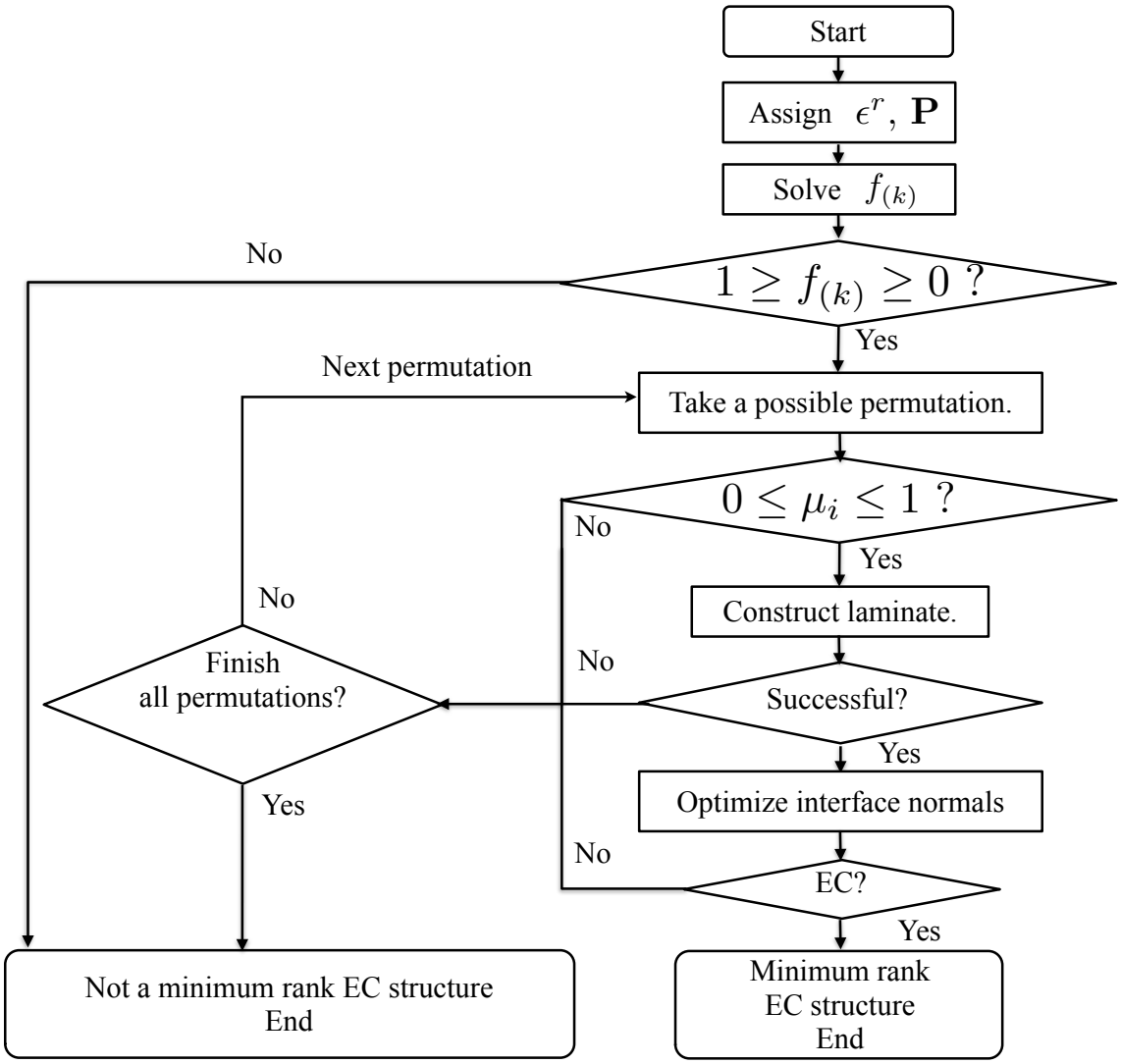

Figure 4.1: Flow chart showing the iteration process for finding minimum rank exactly compatible structures in ferroelectric films.

Next consider distributing the n variants with non-zero $f_{(k)}$ into $2^{\lceil \log_2 n \rceil}$ parts so as to fill the nodal volume fractions in the lowest level of the minimum rank tree diagram. The set of permutations is generated and these are systematically checked. In each step of the iteration, one possible arrangement of the variants is tested. Condition (i), which requires that the volume fraction ratios of certain pairs of nodes are identical, is first checked. If condition (i) cannot be satisfied, then the next permutation is considered. Otherwise, the computation proceeds first to construct a laminate arrangement with compatibility on average, finding the interface normal

vectors $\mathbf{n}_i$ for each of the parent nodes by solving equations (2.6)–(2.8). During the calculation of the interface normal vectors, $\mathbf{n}_i$, the film condition (iv) is checked to ensure $\mathbf{n}_i \nparallel [001]$. When equations (2.6)–(2.8) yield multiple, or even continuous solutions of the interface normals $\mathbf{n}_i$, a strategy similar to that mentioned in section 3.2 is used, to exploit the resulting degrees of freedom so as to satisfy exact compatibility conditions. Once a laminate with average compatibility has been constructed, the remaining exact compatibility conditions (ii) and (iii) are checked. The iteration procedure tests each possible permutation until the conditions (i)–(v) are all satisfied, i.e. an exactly compatible laminate domain structure of minimum rank is found. In this way, a systematic search is made for exactly compatible laminate structures.

4.3 Application to tetragonal films

We now apply the theory and searching procedure to tackle problems relating to single crystal films. In particular, the following questions are of interest:

1. What is the maximum polarization P_{max} that a film with a given crystallographic orientation can achieve while maintaining exact compatibility?

2. Is there a continuous route that the microstructure can follow, starting in an unpoled state ($\mathbf{P} = \mathbf{0}$) and reaching the poled state $P_3 = P_{max}$?

3. What is the influence of substrate strain on the poling behaviour?

To answer these questions, a search can be performed by scanning over the space of possible macroscopic strain and polarization states ($\boldsymbol{\epsilon}^r$, $\mathbf{P}$), seeking compatible domain arrangements. For illustration, $[001]$, $[011]$ and $[111]$ oriented films are considered. The case where the imposed substrate strains $\epsilon^r_{11} = \epsilon^r_{22} = 0$ is shown in sections 4.3.1–4.3.3. The more general application of the method to other states of substrate strain is explored in section 4.3.4.

4.3.1 $[001]$ oriented tetragonal films

The $[001]$ oriented film has the local crystallographic c-axis, $[001]$, of the tetragonal unit cell aligned with the substrate normal, which we define as $[001]$ in the global coordinate system. The six variants of the tetragonal crystal system then have global remanent strain and polarization components as shown in equation (3.4). Alternatively, a more compact expression is used in this chapter as shown in table 4.1, where p^t represents the spontaneous polarization of the unit cell, and β^t is the spontaneous strain magnitude. All shear strain components ϵ_{ij}, $i \neq j$ are zero.

A systematic search for minimum rank, exactly compatible microstructures can be performed by scanning over the space of macroscopic states of polarization $\mathbf{P}$ and strain $\boldsymbol{\epsilon}^r$, and seeking the lowest rank compatible structure at each point. Consider a strain state with $\epsilon^r_{11} = \epsilon^r_{22} = 0$ and using constraint (v) mentioned above, it follows that $\epsilon^r_{33} = 0$. Consequently, all strain components are zero, and the solutions can be shown in (P_1, P_2, P_3) space. The set of points at which there exist solutions to the exact compatibility equations are shown in figure 4.2. The space of possible states of $\mathbf{P}$ that solve equations (2.12)–(2.14), with the imposed substrate strain, is given by the interior of a cube of side $2p^t/3$ centered on the unpoled state ($\mathbf{P} = \mathbf{0}$). This space was first divided into a grid of points with spacing $\frac{1}{90}p^t$ in P_1, P_2 and P_3. Solutions were then found at these points. This allowed several lines in polarization space to be found, which could then be specified exactly by inspection of the points they passed through.

Typical points in the polarization space would require all 6 crystal variants to be present, and could not be achieved by exactly compatible structures. However, several special points which can satisfy exact compatibility conditions are found. For example, point O represents the unpoled state with all 6 variants present; this state allows a rank-3 exactly compatible structure. Figure 4.2 shows several possible routes through polarization space, along which a compatible microstructure can evolve.

Table 4.1: Polarization and strain states of $[001]$ oriented tetragonal crystal variants.

	Variant Number					
	1	2	3	4	5	6
p_1/p^t	1	-1	0	0	0	0
p_2/p^t	0	0	1	-1	0	0
p_3/p^t	0	0	0	0	1	-1
ϵ_{11}/β^t	1	1	-0.5	-0.5	-0.5	-0.5
ϵ_{22}/β^t	-0.5	-0.5	1	1	-0.5	-0.5
ϵ_{33}/β^t	-0.5	-0.5	-0.5	-0.5	1	1

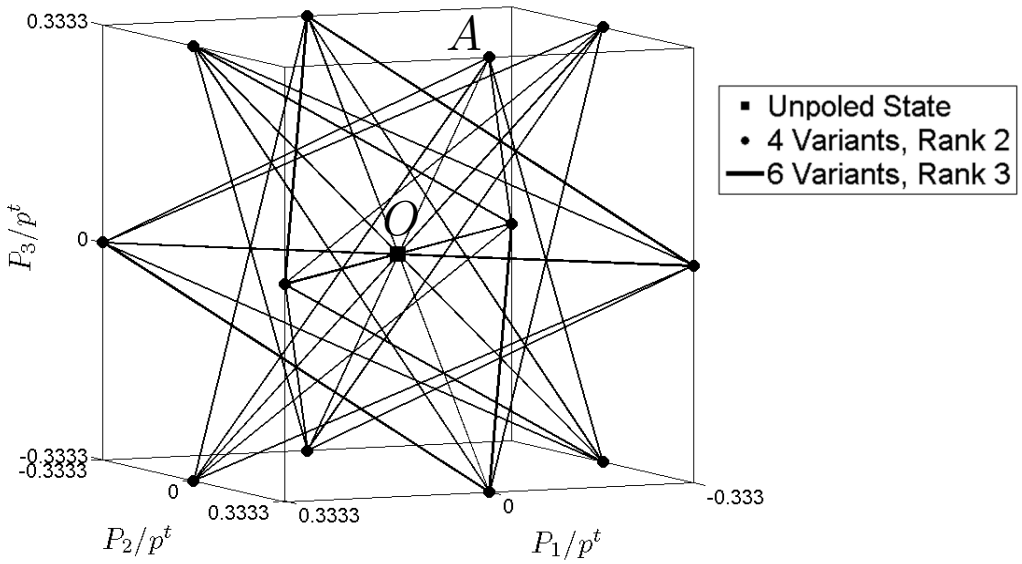

Figure 4.2: The space of possible average polarization in a tetragonal $[001]$ film with substrate constraint.

As for the poling process, the greatest value of macroscopic polarization P_3 that can be achieved in the $[001]$ film with an exactly compatible structure and zero substrate strain is $p^t/3$. Figure 4.2 can be thought of as a map showing the connected paths in polarization space that can be followed without loss of exact compatibility. Interestingly, many continuous paths which can maintain an exactly compatible structure of rank-3 or less, and can achieve the maximal polarization magnitude, are found. For example, the polarization could evolve along line $\overline{OA}$ in figure 4.2. The corresponding microstructure evolution is shown in figure 4.3. Figure 4.3(a) is an exactly compatible microstructure in the unpoled state, with all $f_{(i)} = 1/6$. Six colours/shades

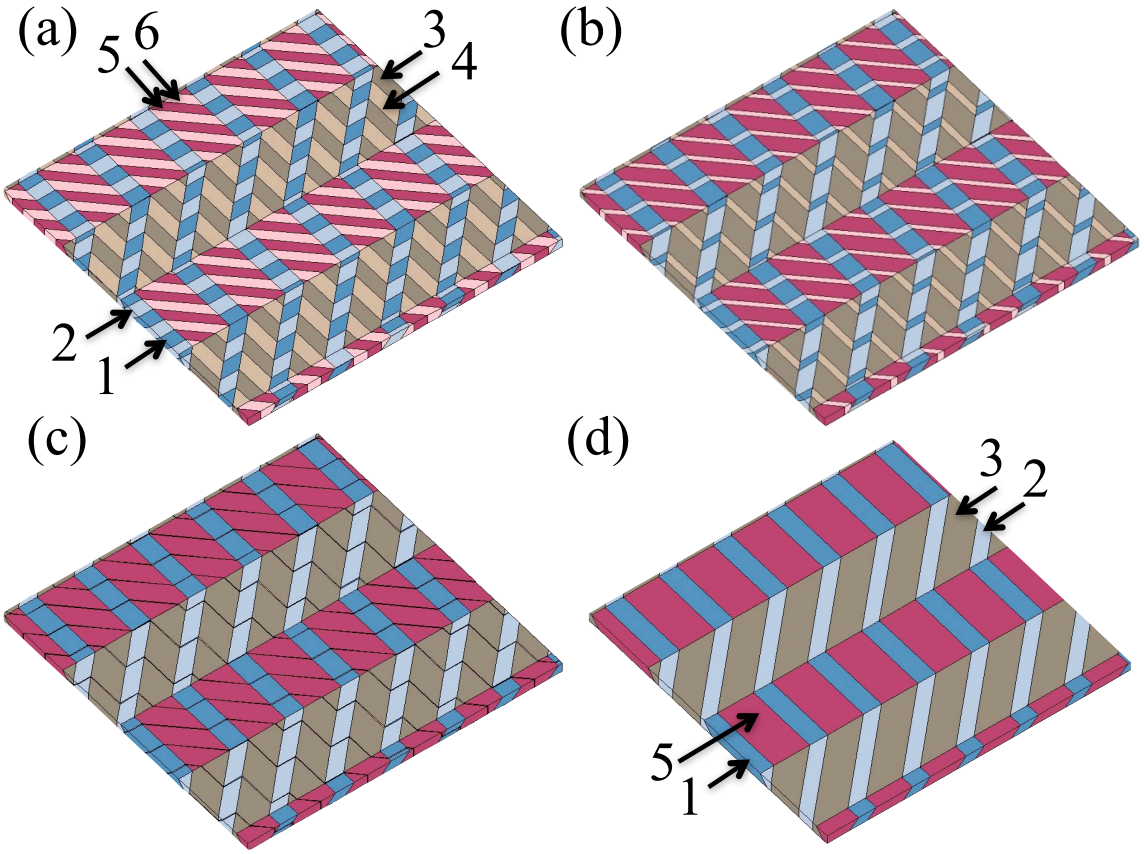

Figure 4.3: The schematic domain evolution in the line $\overline{OA}$ in figure 4.2: (a) unpoled state (b) a typical point on line $\overline{OA}$ (c) $f_{(4)}$ and $f_{(6)}$ decreasing as point A is reached (d) point A where P_3 reaches its extremal value

are used to represent the six distinct crystal variants and the crystal variant numbers are shown using labels. Along path $\overline{OA}$, the total volume fractions $f_{(4)}$ and $f_{(6)}$ decrease steadily – see figures 4.3(b) and (c). Finally, at point A, the domain structure jumps from having 6 variants with a rank-3 microstructure to 4 variants with rank-2 microstructure, as shown in figure 4.3(d). The average polarization components P_2 and P_3 reach their extremal values, $-p^t/3$ and $+p^t/3$ respectively, while all average strain components remain zero. Expressions for the domain volume fractions on line $\overline{OA}$ are shown in table 4.2. The table gives the crystal variant type and associated volume fraction for each of the eight nodes in the lowest level of a rank-3 binary tree diagram. One can obtain the corresponding microstructure at every point on line $\overline{OA}$ by varying x in the range $\frac{1}{12} \leq x \leq \frac{1}{6}$; the microstructure is a rank-3 laminate throughout this

Table 4.2: The crystal variants and volume fraction arrangement on line $\overline{OA}$ in figure 4.2, for the tetragonal $[001]$ films. ($\frac{1}{12} \leq x \leq \frac{1}{6}$)

Node	8	9	10	11	12	13	14	15
Variant	2	1	3	4	1	2	5	6
f_i	x	$\frac{1-6x}{6}$	$2x$	$\frac{1-6x}{3}$	x	$\frac{1-6x}{6}$	$2x$	$\frac{1-6x}{3}$

process, except as x reaches $\frac{1}{6}$. At this point, the volume fractions at nodes 9, 11, 13 and 15 fall to zero and the rank-2 structure at point A is obtained. The tetragonal $[001]$ oriented film is strongly affected by the zero average remanent strain constraint that the substrate imposes, and this limits the through-thickness polarization to $p^t/3$ if compatibility is maintained. Only if the strain clamping effect of the substrate is removed would a low energy, fully-poled, single domain state become possible.

4.3.2 $[011]$ oriented tetragonal films

Next consider a tetragonal film with the local crystallographic $[011]$ direction of the unit cell parallel to the substrate normal (the global $[001]$ direction). When the orientation of the tetragonal unit cell differs from the global $[001]$ direction, the strain and polarization states of the crystal variants can be computed in global coordinates by the use of a coordinate rotation. In general, consider a ferroelectric film with the orientation $\mathbf{r} = [r_1, r_2, r_3]$, where $r_1^2 + r_2^2 + r_3^2 = 1$. The crystallographic axis $\mathbf{r}$ of the unit cell (local coordinates) aligns with the substrate normal ($[001]$ in global coordinates). This coordinate transformation can be achieved by a rotation matrix $\mathbf{R}$, about the axis $[r_2, -r_1, 0]$ in global coordinates, given by

$$\mathbf{R} = \begin{bmatrix} \dfrac{r_1^2 r_3 + r_2^2}{r_1^2 + r_2^2} & \dfrac{-r_1 r_2}{1 + r_3} & -r_1 \\ \dfrac{-r_1 r_2}{1 + r_3} & \dfrac{r_1^2 + r_2^2 r_3}{r_1^2 + r_2^2} & -r_2 \\ r_1 & r_2 & r_3 \end{bmatrix} \tag{4.1}$$

Table 4.3: Polarization and strain states of $[011]$ oriented tetragonal crystal variants.

	Variant Number					
	1	2	3	4	5	6
p_1/p^t	1	-1	0	0	0	0
p_2/p^t	0	0	$1/\sqrt{2}$	$-1/\sqrt{2}$	$-1/\sqrt{2}$	$1/\sqrt{2}$
p_3/p^t	0	0	$1/\sqrt{2}$	$-1/\sqrt{2}$	$1/\sqrt{2}$	$-1/\sqrt{2}$
ϵ_{11}/β^t	1	1	-0.5	-0.5	-0.5	-0.5
ϵ_{22}/β^t	-0.5	-0.5	0.25	0.25	0.25	0.25
ϵ_{23}/β^t	0	0	0.75	0.75	-0.75	-0.75
ϵ_{33}/β^t	-0.5	-0.5	0.25	0.25	0.25	0.25

The resulting strain and polarization states of a $\mathbf{r}$-oriented film are given by $\mathbf{R}\boldsymbol{\epsilon}_{(i)}\mathbf{R}^T$ and $\mathbf{R}\mathbf{p}_{(i)}$, respectively, where the $\boldsymbol{\epsilon}_{(i)}$ and $\mathbf{p}_{(i)}$ are the strain and polarization states in local crystallographic coordinates, which are identical to those shown in table 4.1. Applying this to the tetragonal $[011]$ oriented film, a 45° rotation around the global $[100]$ axis gives the global strain and polarization states of the crystal variants shown in table 4.3, with components that are zero in all crystal variants omitted. A further arbitrary rotation of the crystal variants about the global $[001]$ axis is possible. However, the only case that will be considered here is that in which the imposed substrate strain is axisymmetric, and so the problem is invariant to rotations of the crystal about the global $[001]$ axis.

Based on the set of crystal variant states listed in table 4.3, the set of free variables in macroscopic polarization and remanent strain space can be determined. As with the $[001]$ films, only the case that $\epsilon^r_{11} = \epsilon^r_{22} = 0$ is studied here. Condition (v) gives $\epsilon^r_{33} = 0$, and thus the only nonzero macroscopic remanent strain component is $\epsilon^r_{23} = \epsilon^r_{32}$. Consequently, there are four free variables (P_1, P_2, P_3, ϵ^r_{23}) in the solution space. Inspection of the ϵ_{11} components in table 4.3 shows that the volume fractions of the variants must satisfy the conditions: $f_{(1)} + f_{(2)} = \frac{1}{3}$ and $f_{(3)} + f_{(4)} + f_{(5)} + f_{(6)} = \frac{2}{3}$. These constraints also limit the remanent polarization: the maximum through-thickness polarization P_3 is limited to $\sqrt{2}p^t/3$.

A continuous poling path can be found which achieves a final state $P_3 = \sqrt{2}p^t/3$ and

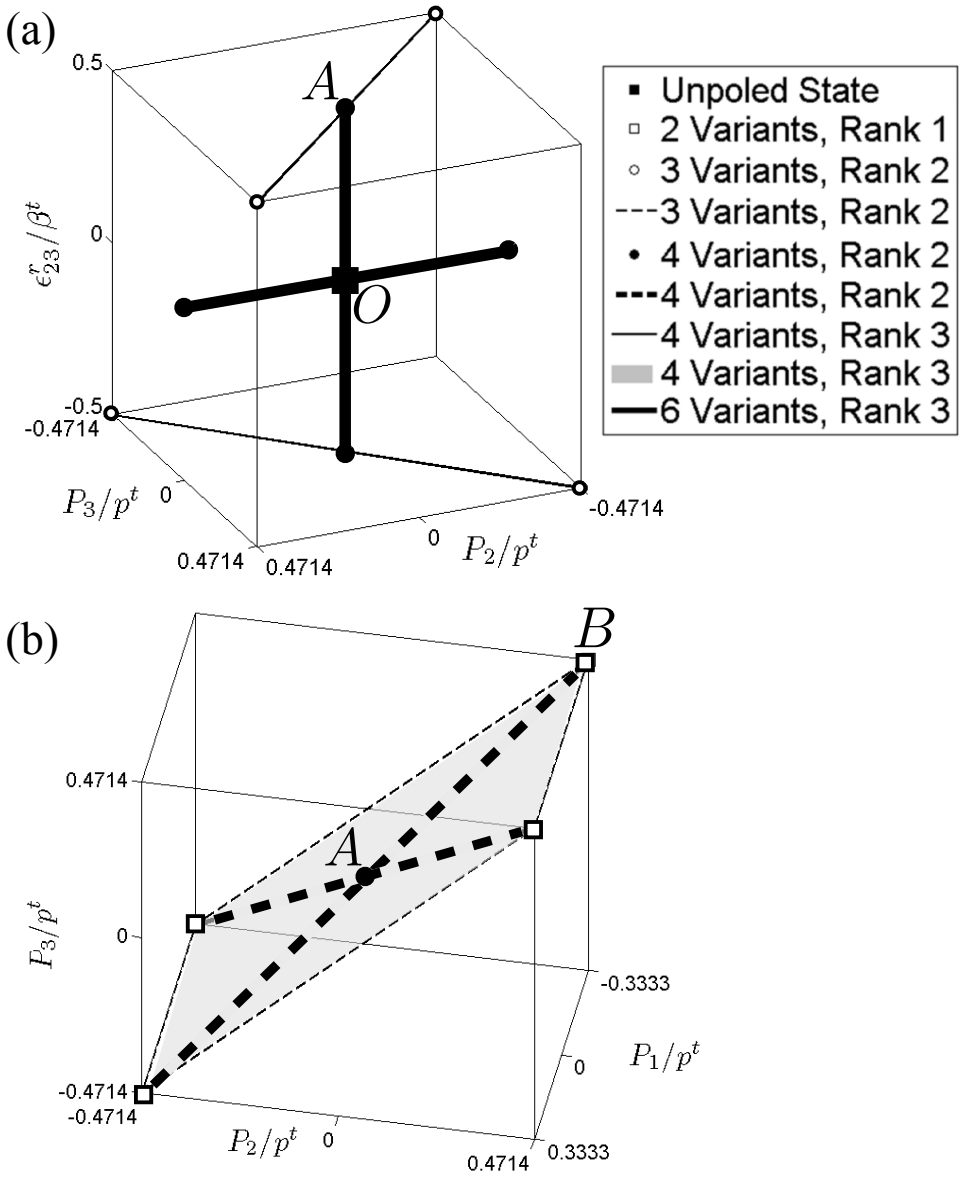

Figure 4.4: The space of possible remanent strain and polarization in a tetragonal $[011]$ film: (a) (P_2, P_3, ϵ^r_{23}) with $P_1 = 0$, and (b) (P_1, P_2, P_3) with $\epsilon^r_{23} = 0.5\beta^t$

maintains exact compatibility. To see this, consider two sections through the 4-dimensional space of the free variables (P_1, P_2, P_3, ϵ^r_{23}). First consider an $[011]$ film maintaining remanent polarization component $P_1 = 0$. The resulting section of polarization-strain space (P_2, P_3, ϵ^r_{23}) is mapped in figure 4.4(a). Exactly compatible solutions in this space are largely eliminated by condition (iv), that $\mathbf{n}_i \neq [001]$. However, several special points can still be found. For example, point O corresponds to the unpoled state with 6 variants and rank-3 exactly compatible structure,

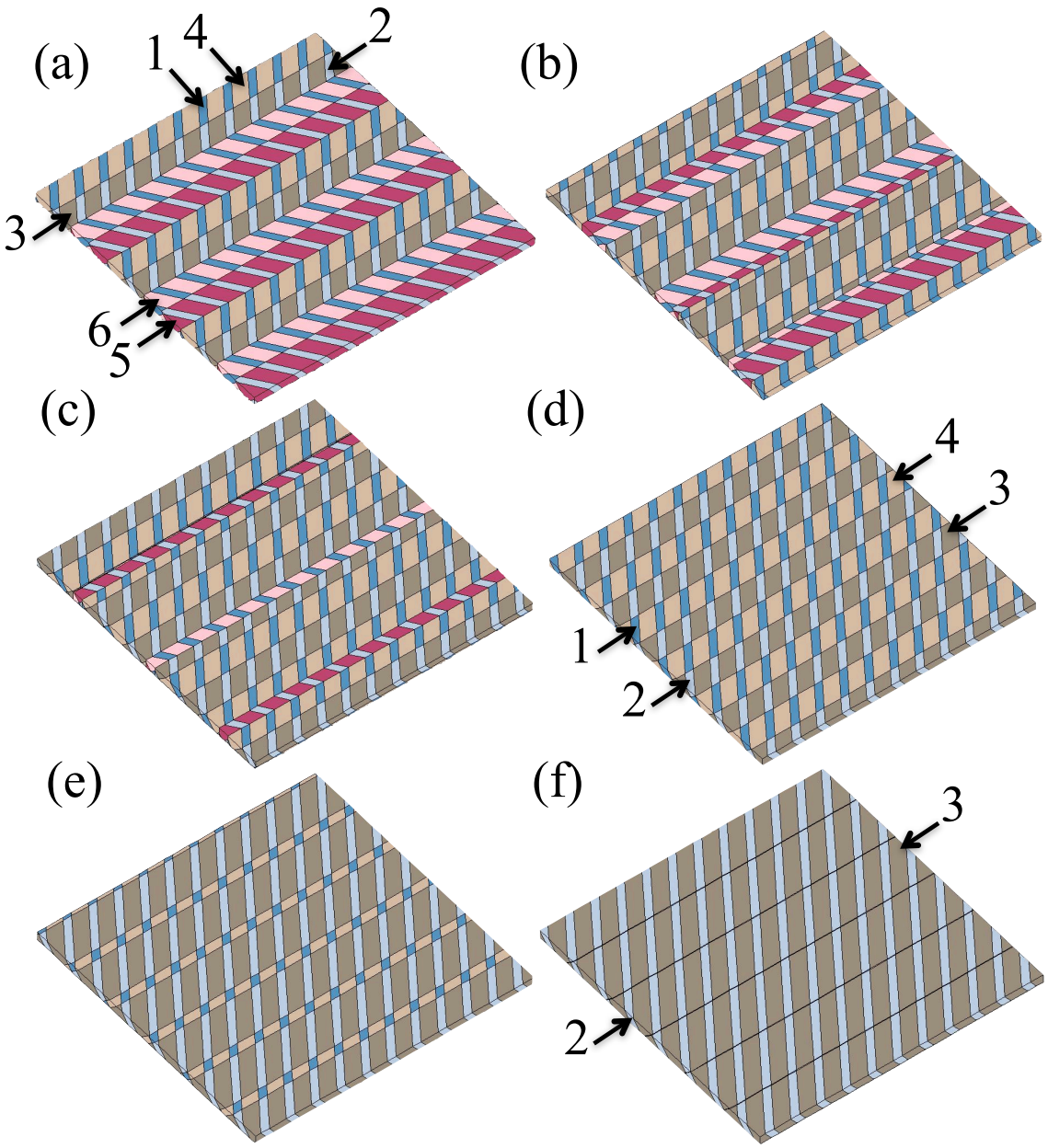

Figure 4.5: The schematic domain evolution in the line $\overline{OA}$ and $\overline{AB}$ in figure 4.4: (a) unpoled state (b) a typical point on line $\overline{OA}$ (c) $f_{(5)}$ and $f_{(6)}$ decreasing as point A is reached (d) point A (e) a typical point on line $\overline{AB}$ (f) point B where P_3 reaches its extremal value.

just as in the case of the $[001]$ film. The domain morphology evolving along the poling path is shown in figure 4.5. Initially the microstructure follows line $\overline{OA}$ of figure 4.4(a), maintaining a rank-3 exactly compatible microstructure. This results in shear straining, $\epsilon^r_{23} > 0$, but no change in polarization. The microstructure evolution is as shown in figure 4.5(a)–(d). When

Table 4.4: The crystal variants and volume fraction arrangement on line $\overline{OA}$ in figure 4.4(a), for the tetragonal $[011]$ films. ($\frac{1}{12} \leq x \leq \frac{1}{6}$)

Node	8	9	10	11	12	13	14	15
Variant	2	3	1	4	1	6	2	5
f_i	x	$2x$	x	$2x$	$\frac{1-6x}{6}$	$\frac{1-6x}{3}$	$\frac{1-6x}{6}$	$\frac{1-6x}{3}$

Table 4.5: The crystal variants and volume fraction arrangement on line $\overline{AB}$ in figure 4.4(b), for the tetragonal $[011]$ films. ($\frac{1}{6} \leq x \leq \frac{1}{3}$)

Node	4	5	6	7
Variant	2	3	1	4
f_i	x	$2x$	$\frac{1-3x}{3}$	$\frac{2-6x}{3}$

the state reaches point A in figure 4.4(a), the volume fractions $f_{(5)}$ and $f_{(6)}$ become zero and the macroscopic strain component ϵ^r_{23} reaches its extremal value $0.5\beta^t$. Next, transfer to the section of polarization-strain space in which the shear strain ϵ^r_{23} maintains a constant value of $0.5\beta^t$. The resulting solution space (P_1, P_2, P_3) is shown in figure 4.4(b) and exhibits an oblique surface on which all points give exactly compatible microstructures. Figure 4.5(d)–(f) show the domain evolution along the line $\overline{AB}$ of figure 4.4(b). Volume fractions $f_{(1)}$ and $f_{(4)}$ decrease as point B is approached. Finally, a rank-2 exactly compatible structure with $P_3 = \sqrt{2}p^t/3$ is formed. Tables 4.4 and 4.5 show the arrangement of variants along the paths $\overline{OA}$ and $\overline{AB}$ of figure 4.4. Note that the first stage of the proposed poling path involves polarization-free straining and thus would be likely to require mechanical loading of the film.

4.3.3 $[111]$ oriented tetragonal films

Now consider a $[111]$ oriented tetragonal film. The remanent strain and polarization states of the variants can be obtained in global coordinates by rotating the states of each variant listed in table 4.1. A rotation of 54.74° about the global $[1\bar{1}0]$ axis gives the polarization and strain states shown in table 4.6. Once again, we consider only the axisymmetric, strain-free substrate

Table 4.6: Polarization and strain states of $[111]$ oriented tetragonal crystal variants.

	Variant Number					
	1	2	3	4	5	6
p_1/p^t	$\frac{3+\sqrt{3}}{6}$	$\frac{-3-\sqrt{3}}{6}$	$\frac{\sqrt{3}-3}{6}$	$\frac{3-\sqrt{3}}{6}$	$-1/\sqrt{3}$	$1/\sqrt{3}$
p_2/p^t	$\frac{\sqrt{3}-3}{6}$	$\frac{3-\sqrt{3}}{6}$	$\frac{3+\sqrt{3}}{6}$	$\frac{-3-\sqrt{3}}{6}$	$-1/\sqrt{3}$	$1/\sqrt{3}$
p_3/p^t	$1/\sqrt{3}$	$-1/\sqrt{3}$	$1/\sqrt{3}$	$-1/\sqrt{3}$	$1/\sqrt{3}$	$-1/\sqrt{3}$
ϵ_{11}/β^t	$\sqrt{3}/4$	$\sqrt{3}/4$	$-\sqrt{3}/4$	$-\sqrt{3}/4$	0	0
ϵ_{12}/β^t	$-1/4$	$-1/4$	$-1/4$	$-1/4$	$1/2$	$1/2$
ϵ_{13}/β^t	$\frac{\sqrt{3}+1}{4}$	$\frac{\sqrt{3}+1}{4}$	$\frac{1-\sqrt{3}}{4}$	$\frac{1-\sqrt{3}}{4}$	$-1/2$	$-1/2$
ϵ_{22}/β^t	$-\sqrt{3}/4$	$-\sqrt{3}/4$	$\sqrt{3}/4$	$\sqrt{3}/4$	0	0
ϵ_{23}/β^t	$\frac{1-\sqrt{3}}{4}$	$\frac{1-\sqrt{3}}{4}$	$\frac{\sqrt{3}+1}{4}$	$\frac{\sqrt{3}+1}{4}$	$-1/2$	$-1/2$

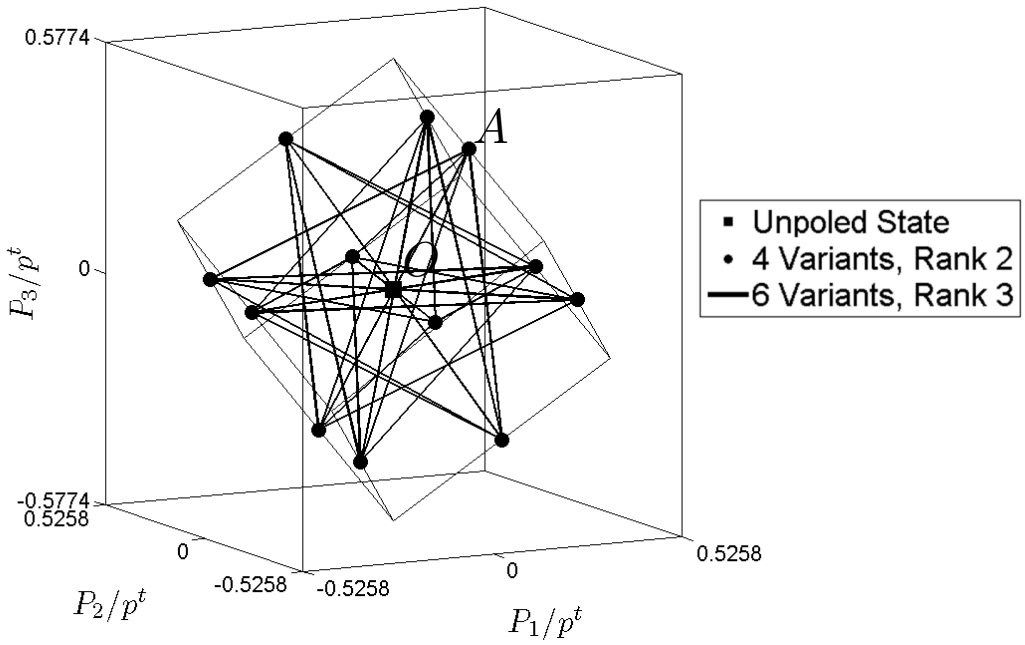

Figure 4.6: The space of possible average polarization in a tetragonal $[111]$ film.

condition $\epsilon^r_{11} = \epsilon^r_{22} = 0$, such that the problem is invariant to rotations around the global $[001]$ axis. By applying condition (v), and considering the rows of table 4.6 for ϵ^r_{11}, ϵ^r_{12} and ϵ^r_{22}, the total volume fractions are found to satisfy: $f_{(1)} + f_{(2)} = f_{(3)} + f_{(4)} = f_{(5)} + f_{(6)} = \frac{1}{3}$. It follows from table 4.6 that all components of the macroscopic remanent strain $\boldsymbol{\epsilon}^r$ are equal to zero. Thus there are only three free variables (P_1, P_2, P_3).

The solution space is shown in figure 4.6, and includes a set of lines joining the unpoled

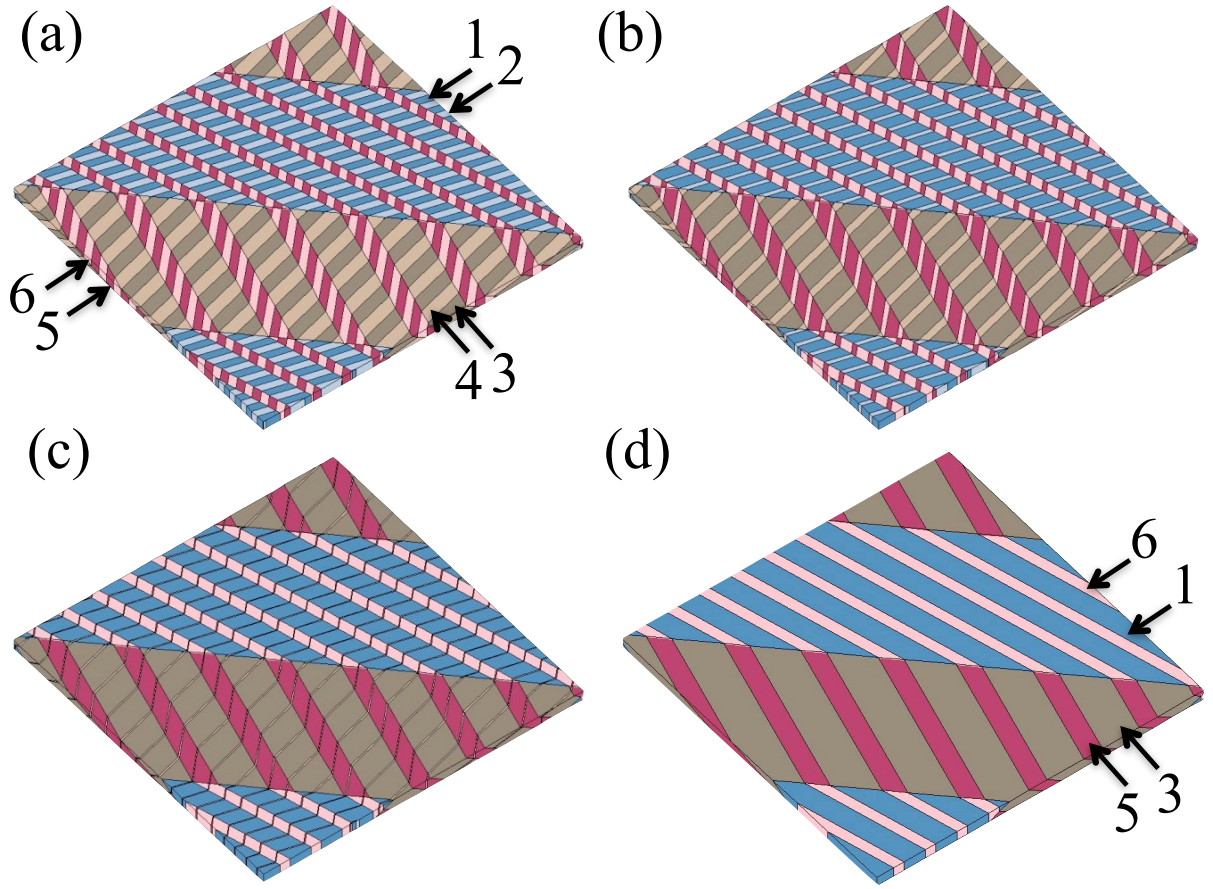

Figure 4.7: The schematic domain evolution in the line $\overline{OA}$ in figure 4.6: (a) unpoled state (b) a typical point on line $\overline{OA}$ (c) $f_{(2)}$ and $f_{(4)}$ are decreasing as point A is reached (d) point A where P_3 reaches $2/3$ of its extremal value

Table 4.7: The crystal variants and volume fraction arrangement on line $\overline{OA}$ in figure 4.6, for the tetragonal $[111]$ films. $(0 \leq x \leq \frac{1}{12})$

Node	8	9	10	11	12	13	14	15
Variant	5	6	2	1	6	5	4	3
f_i	x	$\frac{1-6x}{6}$	$2x$	$\frac{1-6x}{3}$	x	$\frac{1-6x}{6}$	$2x$	$\frac{1-6x}{3}$

state, O, to the edge-centres of a cube-shaped domain of possible polarization states. In total there are 12 such lines; 6 of these give no change in the through-thickness component of macroscopic remanent polarization as they lie in the plane $P_3 = 0$. It is interesting to note that the exactly compatible states are a rotation of those of the $[001]$ films, which were shown in figure 4.2. The maximum value of through-thickness polarization that can be achieved in this

system while maintaining exact compatibility is $2p^t/(3\sqrt{3})$. This is reached by following any of three symmetrically related lines, such as $\overline{OA}$ in figure 4.6. The microstructural evolution is similar to that discussed in the context of the $[001]$ oriented film. However, since the microstructure is rotated relative to the $[001]$ case, a different pattern of domains appears at the film surface, as shown in figure 4.7. The domain volume fractions and crystal variant arrangement is shown in table 4.7 and is a permutation of the corresponding $[001]$ case. Thus, subject to the strong constraint of clamping to zero strain by the substrate, and remaining compatible, the $[111]$ film achieves a greater polarization than the $[001]$ film.

4.3.4 Influence of substrate strain on poling paths in $[001]$ tetragonal films.

The relationship between film orientation and poling behaviour in constrained tetragonal films has been discussed in sections 4.3.1–4.3.3. Consider how the poling behaviour depends on the macroscopic strain imposed by the substrate. For the purpose of illustration, the influence of strain on an [001] oriented tetragonal film is studied. The methods are equally applicable to other cases.

The $[001]$ oriented tetragonal crystal system has 6 crystal variants with the strain and polarization states that were given in table 4.1. Now consider the case that the substrate imposes the axisymmetric strain condition $\epsilon^r_{11} = \epsilon^r_{22} = \epsilon_{ax}$, where ϵ_{ax} is the imposed in-plane biaxial strain. Such strains could arise during manufacture due to epitaxial mismatch or thermal mismatch between the film and the substrate; alternatively they could be induced by biaxial curvature of the substrate. Given the isochoric nature of remanent straining, $\epsilon^r_{33} = -\epsilon^r_{11} - \epsilon^r_{22}$; hence ϵ_{ax} is limited to the range $-0.5\beta^t$ to $0.25\beta^t$ if the film is to be able to accommodate the strain as an average remanent strain. Thus there are only 4 free variables to consider in the space of macroscopic strain and polarization: P_1, P_2, P_3, and ϵ_{ax}. For each point in this space, equations (2.12)–(2.14) give a unique solution for the total volume fraction of each crystal variant.

A search for minimum rank exactly compatible domain arrangements was conducted in the polarization space (P_1, P_2, P_3) with different values of imposed strain, scanning the full range of axisymmetric strain states ($-0.5 \leq \epsilon_{ax}/\beta^t \leq 0.25$). Poling maps at through-thickness strain values of $\epsilon_{ax}/\beta^t = 0.25,\ 0.15,\ 0,\ -0.05,\ -0.25,\ -0.5$ are shown in figure 4.8. The typical form of these poling maps (see figure 4.8(b), (d) and (e)) contains 20 vertices, connected by 34 lines. Of these 34 lines, 32 connect 16 vertices with a nonzero polarization P_3, while 2 lines, which meet at the central point ($\mathbf{P} = \mathbf{0}$), connect 4 further vertices lying in the plane $P_3 = 0$. Each of the 20 vertices represents a state with 4 variants present in a rank-2 exactly compatible domain structure. Points on the 34 connecting lines have all 6 variants present in a rank-3 exactly compatible structure. This complicated set of points and lines can be interpreted more simply as 5 basic lines connecting a group of 6 points (see figure 4.9(b), (d) and (e)) which are then subjected to the set of symmetry elements of the $4mm$ crystal class to generate the full poling maps of figure 4.8.

Of the 5 basic lines, 4 lines connect a point $\mathbf{v}^{(0)}$ with each of 4 points $\mathbf{v}^{(1)}$ to $\mathbf{v}^{(4)}$, while a fifth line connects the central point ($\mathbf{P} = \mathbf{0}$) with a further point $\mathbf{v}^{(5)}$. The coordinates of points $\mathbf{v}^{(0)}$ to $\mathbf{v}^{(5)}$ in normalized polarization space are given by

$$\begin{aligned} &\mathbf{v}^{(0)} = [v_1, v_2, v_3] \qquad &&\mathbf{v}^{(1)} = [v_2, v_1, -v_3] \qquad &&\mathbf{v}^{(2)} = [-v_1, v_2, -v_3] \\ &\mathbf{v}^{(3)} = [-v_1, -v_2, -v_3] \qquad &&\mathbf{v}^{(4)} = [-v_2, -v_1, -v_3] \qquad &&\mathbf{v}^{(5)} = [-v_1, v_1, 0] \end{aligned} \tag{4.2}$$

where

$$v_1 = \frac{1 + 2\epsilon_{ax}/\beta^t}{3}, \quad v_2 = \frac{2(\epsilon_{ax}/\beta^t)^2 + \epsilon_{ax}/\beta^t}{1 - \epsilon_{ax}/\beta^t} \quad \text{and} \quad v_3 = \frac{1 - 4\epsilon_{ax}/\beta^t}{3}. \tag{4.3}$$

At certain special values of ϵ_{ax} the topology of the poling map changes. When $\epsilon_{ax}/\beta^t = 0.25$ the film is dilated as far as possible in-plane and only those variants with in-plane polarization are present. Then points $\mathbf{v}^{(0)}$ and $\mathbf{v}^{(1)}$ coincide, as do points ($\mathbf{v}^{(2)}$,$\mathbf{v}^{(5)}$), and also points ($\mathbf{v}^{(3)}$,$\mathbf{v}^{(4)}$).

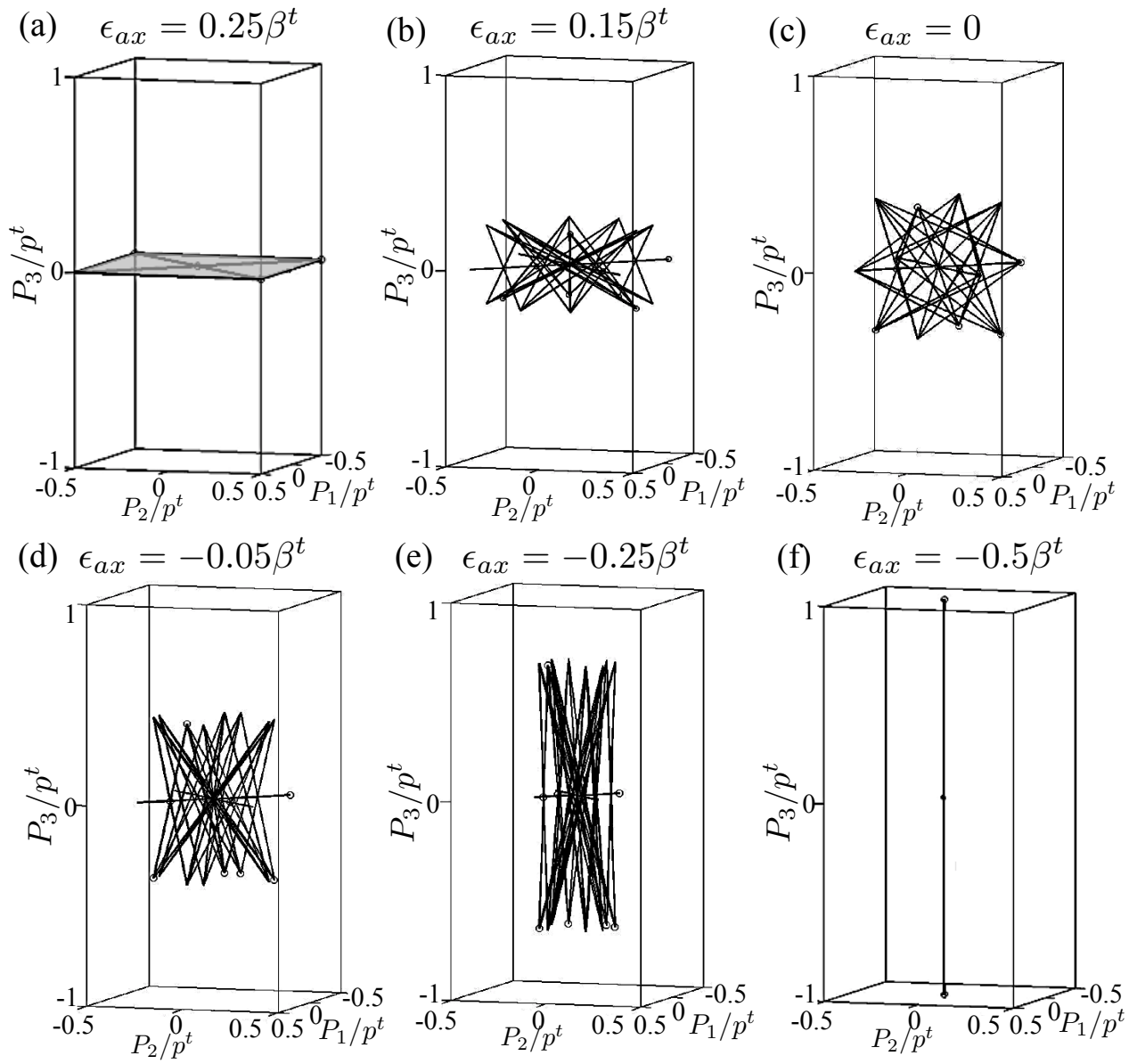

Figure 4.8: Poling maps for an [001] oriented tetragonal film, computed with various states of axisymmetric strain, characterized by ϵ_{ax}: (a) $\epsilon_{ax} = 0.25\beta^t$ (b) $\epsilon_{ax} = 0.15\beta^t$ (c) $\epsilon_{ax} = 0$ (d) $\epsilon_{ax} = -0.05\beta^t$ (e) $\epsilon_{ax} = -0.25\beta^t$ (f) $\epsilon_{ax} = -0.5\beta^t$.

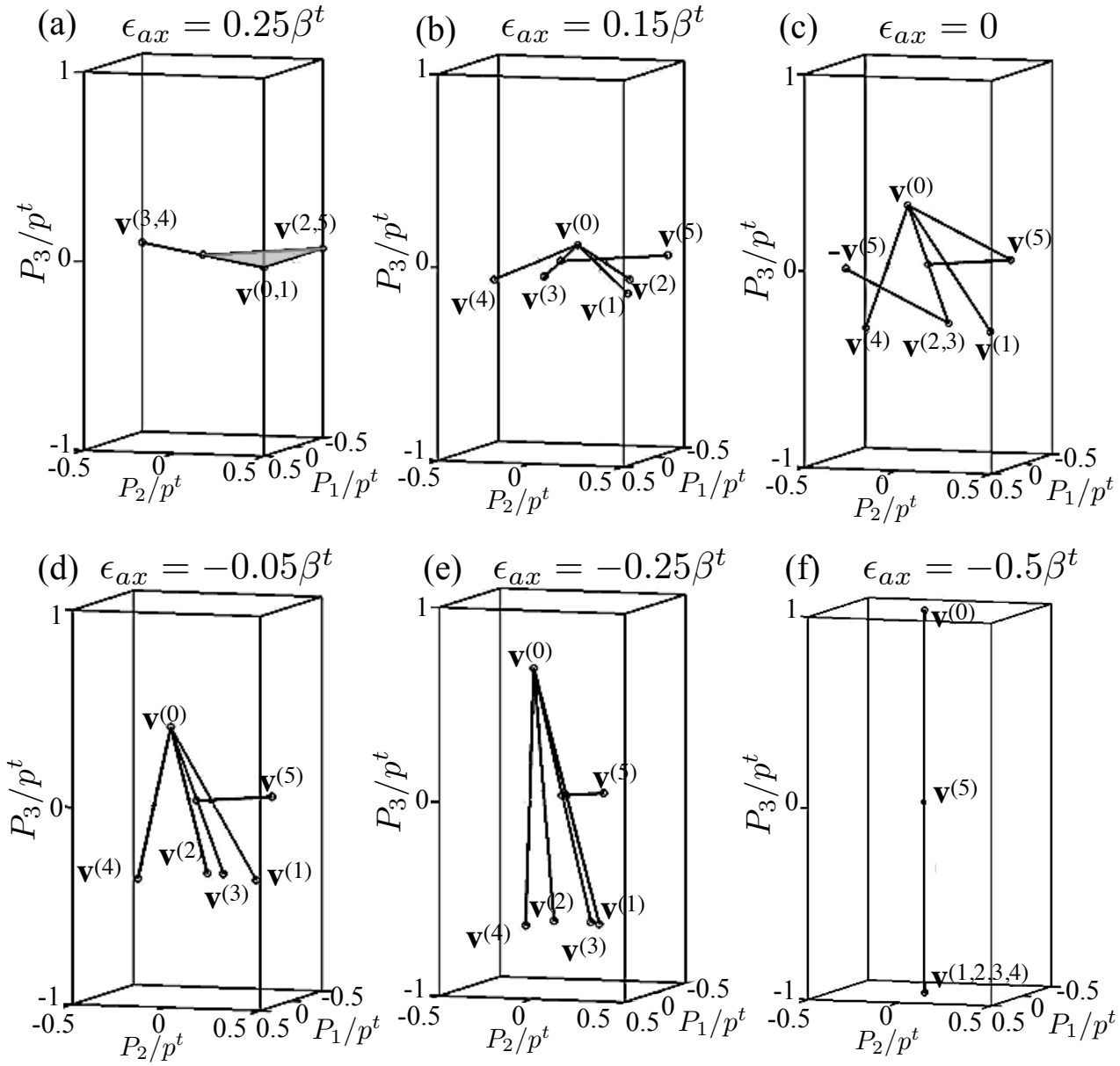

Figure 4.9: The evolution of basic lines, which can generate the entire poling map as the map shown in figure 4.8 by $4mm$ symmetry operations. The generating lines are shown at various ϵ_{ax} values: (a) $\epsilon_{ax} = 0.25\beta^t$ (b) $\epsilon_{ax} = 0.15\beta^t$ (c) $\epsilon_{ax} = 0$ (d) $\epsilon_{ax} = -0.05\beta^t$ (e) $\epsilon_{ax} = -0.25\beta^t$ (f) $\epsilon_{ax} = -0.5\beta^t$.

This strain state corresponds to figures 4.8(a) and 4.9(a); in this special case, all of the accessible points in the plane $P_3 = 0$ allow exactly compatible domain arrangements of rank-3 or less, with 4 variants present. However, there are no exactly compatible states with non-zero through-thickness polarization: the substrate constraint prevents the film from being poled.

When $\epsilon_{ax} = 0$, another special case occurs, see figures 4.8(c) and 4.9(c). Here, points $\mathbf{v}^{(2)}$ and $\mathbf{v}^{(3)}$ become coincident, but a pair of new lines appear, connecting $\mathbf{v}^{(0)}$ to $\mathbf{v}^{(5)}$ and $\mathbf{v}^{(2)}$ to $-\mathbf{v}^{(5)}$. All of the lines represent states which allow rank-3 exactly compatible structures with all 6 variants present. Curiously, the resulting pattern of lines in figure 4.8(c) forms a stellated dodecahedron. Also, note that this case of substrate strain has been discussed in section 4.3.1, and thus figure 4.8(c) in fact shows an identical map as the one shown in figure 4.2.

A final special case occurs when ϵ_{ax}/β^t reaches its extreme negative value of -0.5, see figures 4.8(f) and 4.9(f). Then, only those crystal variants with out-of-plane remanent polarization are present in the film. Points $\mathbf{v}^{(1)}$ to $\mathbf{v}^{(4)}$ become coincident and point $\mathbf{v}^{(5)}$ reaches the polarization-free centre. The resulting topology of the poling map becomes a single straight line with $P_1 = P_2 = 0$.

Having described the complicated geometry of the poling maps in figure 4.8, let us now consider what they indicate about the maximal state of through-thickness polarization that can be achieved in $[001]$ oriented tetragonal films while maintaining exactly compatible microstructure. Notice that the P_3 component of the point $\mathbf{v}^{(0)}$, with value v_3, gives the greatest magnitude of normalized through-thickness polarization in each diagram. Thus the maximum value of through thickness polarization can be expressed in terms of the imposed axisymmetric strain ϵ_{ax} as

$$P_{max} = \frac{1 - 4\epsilon_{ax}/\beta^t}{3} p^t \tag{4.4}$$

Figure 4.9 also allows us to find poling paths that connect a polarization-free initial state to a poled state with $P_3 = P_{max}$. A poling path exists at each value of axisymmetric strain because the point $\mathbf{P} = \mathbf{0}$ is always connected to point $\mathbf{v}^{(0)}$ by a straight line representing rank-3 structure.

Compatible poling routes exist for [001] tetragonal films at all states of imposed axisymmetric strain, and the greatest polarization is achieved with in-plane compression.

4.4 Application to rhombohedral films

We now apply the same theory and searching procedure to the rhombohedral crystal system, which produces the added complication that the variant volume fractions derived from equations (2.12)–(2.14) are non-unique. For illustration, the case where the imposed substrate strains ϵ^r_{11}, ϵ^r_{22}, and ϵ^r_{12} are all zero is shown in this section.

In the rhombohedral crystal system, there are eight crystal variants with the strain $\boldsymbol{\epsilon}_{(i)}$, $(i = 1 \ldots 8)$ and polarization $\mathbf{p}_{(i)}$ given by equation (3.7). Parameters α^{rh}, β^{rh}, and p^{rh} characterize the material, but the choice of a reference state for strain with $\mathrm{tr}(\boldsymbol{\epsilon}_i) = 0$ forces $\alpha^{rh} = 0$ and so eliminates this parameter. For a rhombohedral film with average remanent strain $\boldsymbol{\epsilon}^r$ and polarization $\mathbf{P}$, equations (2.12)–(2.14) produce 7 equations for 8 unknown volume fractions, giving a general solution as shown in equation (3.10). Similar to the method used in section 3.4, only three cases are considered here: $\gamma = 0$, $\gamma_{max}/2$ and γ_{max}. It is worth reminding ourselves that when $\gamma = 0$ or γ_{max}, at least one crystal variant has zero volume fraction, resulting in a minimum number of variants being present. Conversely, when $\gamma = \gamma_{max}/2$, the number of variants present is maximized, and at least two variants have equal volume fractions, producing a symmetrical arrangement.

4.4.1 $[001]$ oriented rhombohedral film

In the $[001]$ oriented film, the rhombohedral crystal is grown on the substrate such that the local crystallographic $[001]$ axis is normal to the substrate. In this case the local crystallographic coordinates and the global coordinates, aligned with the film, are identical. The global strain and polarization components of the 8 crystal variants are then as shown in table 4.8. The diagonal

Table 4.8: Polarization and strain states of the [001] oriented rhombohedral crystal variants in global coordinates.

	Variant Number							
	1	2	3	4	5	6	7	8
p_1/p^{rh}	$1/\sqrt{3}$	$-1/\sqrt{3}$	$-1/\sqrt{3}$	$1/\sqrt{3}$	$-1/\sqrt{3}$	$1/\sqrt{3}$	$1/\sqrt{3}$	$-1/\sqrt{3}$
p_2/p^{rh}	$1/\sqrt{3}$	$-1/\sqrt{3}$	$1/\sqrt{3}$	$-1/\sqrt{3}$	$-1/\sqrt{3}$	$1/\sqrt{3}$	$-1/\sqrt{3}$	$1/\sqrt{3}$
p_3/p^{rh}	$1/\sqrt{3}$	$-1/\sqrt{3}$	$1/\sqrt{3}$	$-1/\sqrt{3}$	$1/\sqrt{3}$	$-1/\sqrt{3}$	$1/\sqrt{3}$	$-1/\sqrt{3}$
ϵ_{12}/β^{rh}	1	1	-1	-1	1	1	-1	-1
ϵ_{13}/β^{rh}	1	1	-1	-1	-1	-1	1	1
ϵ_{23}/β^{rh}	1	1	1	1	-1	-1	-1	-1

strain components ϵ_{ij} $(i = j)$ are all zero and so have been omitted. Since the case under consideration has zero in-plane strain imposed by the substrate, there remain just 5 free variables in the space of ($\boldsymbol{\epsilon}^r$, $\mathbf{P}$), namely ϵ^r_{13}, ϵ^r_{23}, P_1, P_2 and P_3. The search procedure was applied over the space of these 5 free variables.

Using a method similar to that of section 4.3, the most polarized state of the film was identified, having $P_{max} = p^{rh}/\sqrt{3}$. This state can be achieved with either $P_1 = 0$ and $\epsilon^r_{13} = 0$ or with $P_2 = 0$ and $\epsilon^r_{23} = 0$. By focusing attention on the macroscopic states which maintain $P_2 = 0$ and $\epsilon^r_{23} = 0$, the search space reduces to 3 free variables $(P_1, P_3, \epsilon^r_{13})$ and is easier to visualize, as shown in figure 4.10. The tetrahedral region $CBFH$ in figure 4.10 is the space of all solutions to equations (2.12)–(2.14) subjected only to the constraint $f_{(k)} \geq 0$. However, general points within this space violate condition (iv) by having domain walls parallel to the substrate, and so do not allow exactly compatible periodic microstructure in a film. Nevertheless, several points and lines corresponding to exactly compatible states in region $CBFH$ can be found. Point O is representative of a rhombohedral crystal in an unpoled state and allows an exactly compatible domain arrangement of rank-3, wherein all 8 crystal variants have equal volume fraction. The state can evolve from point O while maintaining rank-3 exactly compatible structure by moving along any of the lines $\overline{OA}$, $\overline{OD}$, $\overline{OE}$, or $\overline{OG}$. Meanwhile, the lines $\overline{FAH}$ and $\overline{BGC}$ connect states that require 6 variants and rank-3 structure. Points on the dashed lines

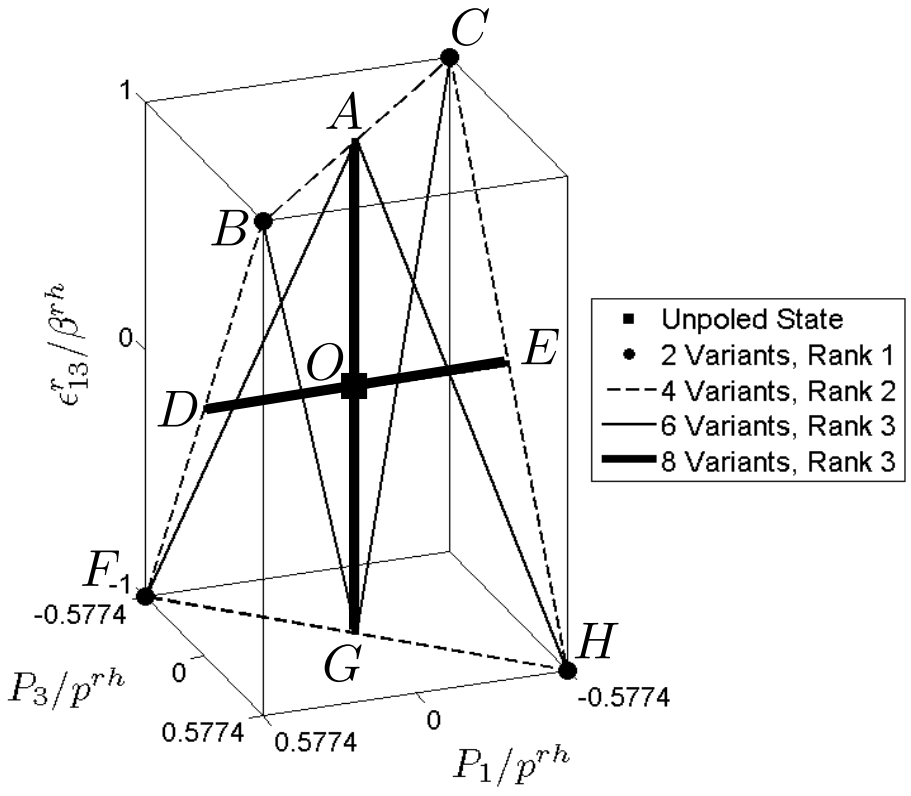

Figure 4.10: The exactly compatible states in the space of possible macroscopic strain and polarization of a rhombohedral $[001]$ film.

$\overline{CB}$, $\overline{BF}$, $\overline{FH}$, and $\overline{HC}$ admit rank-2 exactly compatible structure with only 4 variants present. These dashed lines connect the 4 extremal points C, B, F and H each of which represents a state with only 2 variants present. Points B and H are poled states, each having $P_3 = P_{max}$.

Figure 4.10 suggests some interesting poling routes for the rhombohedral $[001]$ film: for example, poling could be achieved by following the path $O \rightarrow A \rightarrow B$. This consists of shear straining to increase ϵ^r_{13} along path $\overline{OA}$, without imposing any polarization changes, followed by strain-free $180°$, switching along $\overline{AB}$. This is an unconventional poling route, in which part of the process involves mechanical deformation so as to maximize the poling ability of the film. The domain evolution during this hypothetical poling process is shown in figure 4.11. Eight colours/shades are used to represent the 8 distinct rhombohedral crystal variants. Remarkably, the intersections of the domain walls with the film surface appear as a set of parallel lines during this process. However, the domain walls themselves are not parallel planes as the domain

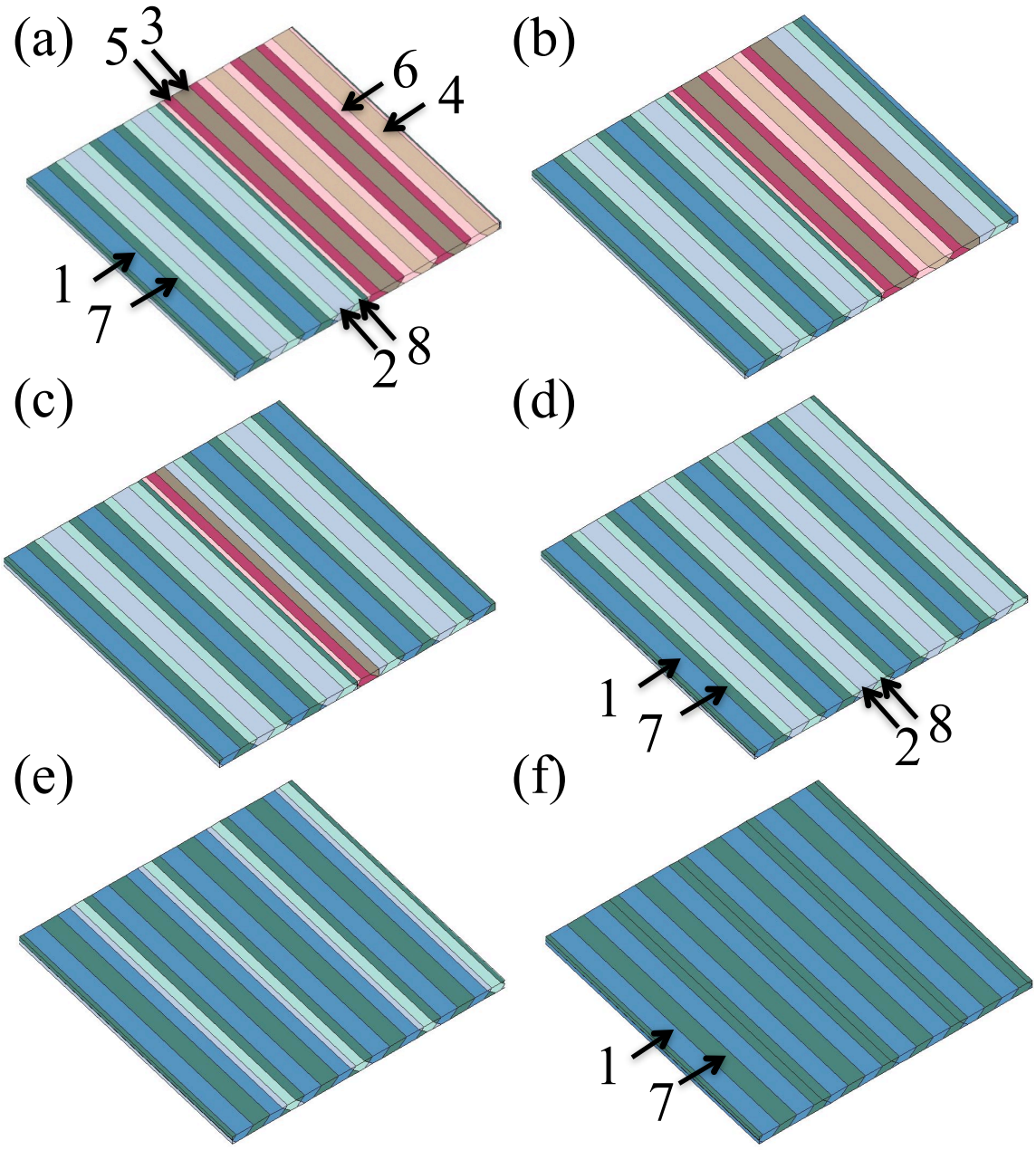

Figure 4.11: The schematic domain evolution along the path $O \rightarrow A \rightarrow B$ in figure 4.10: (a) unpoled state (b) a typical point on line $\overline{OA}$ (c) as point A is almost reached (d) at point A (e) a typical point on line $\overline{AB}$ (f) point B, where the through-thickness polarization P_3 reaches its extremal value.

Table 4.9: The arrangement of crystal variants and volume fractions on line $\overline{OA}$ in figure 4.10. ($\frac{1}{8} \leq x \leq \frac{1}{4}$)

Node	8	9	10	11	12	13	14	15
Variant	4	6	3	5	1	7	2	8
f_i	$\frac{1}{4}-x$	$\frac{1}{4}-x$	$\frac{1}{4}-x$	$\frac{1}{4}-x$	x	x	x	x

Table 4.10: The arrangement of crystal variants and volume fractions on line $\overline{AB}$ in figure 4.10. ($\frac{1}{4} \leq x \leq \frac{1}{2}$)

Node	4	5	6	7
Variant	1	7	2	8
f_i	x	x	$\frac{1}{2}-x$	$\frac{1}{2}-x$

wall normals are tilted in differing directions. Figure 4.11(a) is an exactly compatible domain arrangement in the unpoled state with all 8 variants present in equal volume fractions. The same arrangement is also shown in Shu *et al.* [13]. Figure 4.11(b)–(d) show that the microstructure gradually decreases the total volume fraction of rhombohedral variants 3, 4, 5 and 6 and there is a sudden jump from rank-3 to rank-2 structure when these 4 variants vanish completely (figure 4.11(d)). Finally, variants 2 and 8 undergo 180° switching into variants 1 and 7 until the poled state is achieved (figure 4.11(f)). Expressions for the variant arrangement and nodal volume fractions in the bottom level of the tree diagram as lines $\overline{OA}$ and $\overline{AB}$ are traversed can be obtained by inspection, and are shown in tables 4.9 and 4.10. One can obtain the variant arrangement of any point along the path $O \rightarrow A \rightarrow B$ by altering the value of x within the ranges provided in tables 4.9 and 4.10.

4.4.2 $[011]$ oriented rhombohedral film

Consider a $[011]$ oriented rhombohedral film: the global strain and polarization states of the crystal variants are shown in table 4.11. Some components are omitted from the table as their values are zero for all variants. As with the $[001]$ oriented films, the case of a rigid

Table 4.11: Polarization and strain states of the $[011]$ oriented rhombohedral crystal variants in global coordinates.

	Variant Number							
	1	2	3	4	5	6	7	8
p_1/p^{rh}	$1/\sqrt{3}$	$-1/\sqrt{3}$	$-1/\sqrt{3}$	$1/\sqrt{3}$	$-1/\sqrt{3}$	$1/\sqrt{3}$	$1/\sqrt{3}$	$-1/\sqrt{3}$
p_2/p^{rh}	0	0	0	0	$-\sqrt{6}/3$	$\sqrt{6}/3$	$-\sqrt{6}/3$	$\sqrt{6}/3$
p_3/p^{rh}	$\sqrt{6}/3$	$-\sqrt{6}/3$	$\sqrt{6}/3$	$-\sqrt{6}/3$	0	0	0	0
ϵ_{12}/β^{rh}	0	0	0	0	$\sqrt{2}$	$\sqrt{2}$	$-\sqrt{2}$	$-\sqrt{2}$
ϵ_{13}/β^{rh}	$\sqrt{2}$	$\sqrt{2}$	$-\sqrt{2}$	$-\sqrt{2}$	0	0	0	0
ϵ_{22}/β^{rh}	-1	-1	-1	-1	1	1	1	1
ϵ_{33}/β^{rh}	1	1	1	1	-1	-1	-1	-1

constraint with zero in-plane strain is considered, so that $\epsilon^r_{11} = \epsilon^r_{22} = \epsilon^r_{12} = 0$. This limits the volume fraction composition: inspection of the ϵ_{22} components in table 4.11 shows that $f_{(1)} + f_{(2)} + f_{(3)} + f_{(4)} = 1/2$, while further inspection of the ϵ_{12} components gives $f_{(5)}+f_{(6)} = f_{(7)} + f_{(8)} = 1/4$. Now considering the p_3 components, it follows from these volume fraction constraints that the value of through-thickness macroscopic remanent polarization, P_3, cannot be greater than $\sqrt{6}p^{rh}/6$. The space of macroscopic states has 4 free variables: P_1, P_2, P_3, ϵ^r_{13}. However, poling paths connecting the unpoled state with a state where $P_3 = \sqrt{6}p^{rh}/6$ can be found in a space with only the three free variables (P_1, P_2, P_3), holding $\epsilon^r_{13} = 0$, so attention is focused on this reduced space.

Figure 4.12 shows the set of points in (P_1, P_2, P_3) space which allow minimum rank exactly compatible domain arrangements with $\epsilon^r_{13} = 0$. Again, typical points inside the region of figure 4.12 violate the condition (iv) and thus do not allow a periodic laminate structure in the film. It is worth noting that macroscopic polarization component P_1 can achieve a greater value ($p^{rh}/\sqrt{3}$) than that of the through-thickness polarization component P_3 ($\sqrt{6}p^{rh}/6$) or the traverse polarization component P_2 ($\sqrt{6}p^{rh}/6$). Points at which one or more polarization components reach extremal values are A, B, C, D, E, and F. They are connected by three lines $\overline{AF}$, $\overline{CE}$, and $\overline{BD}$, which meet at the unpoled state O. Thus the domain arrangement can

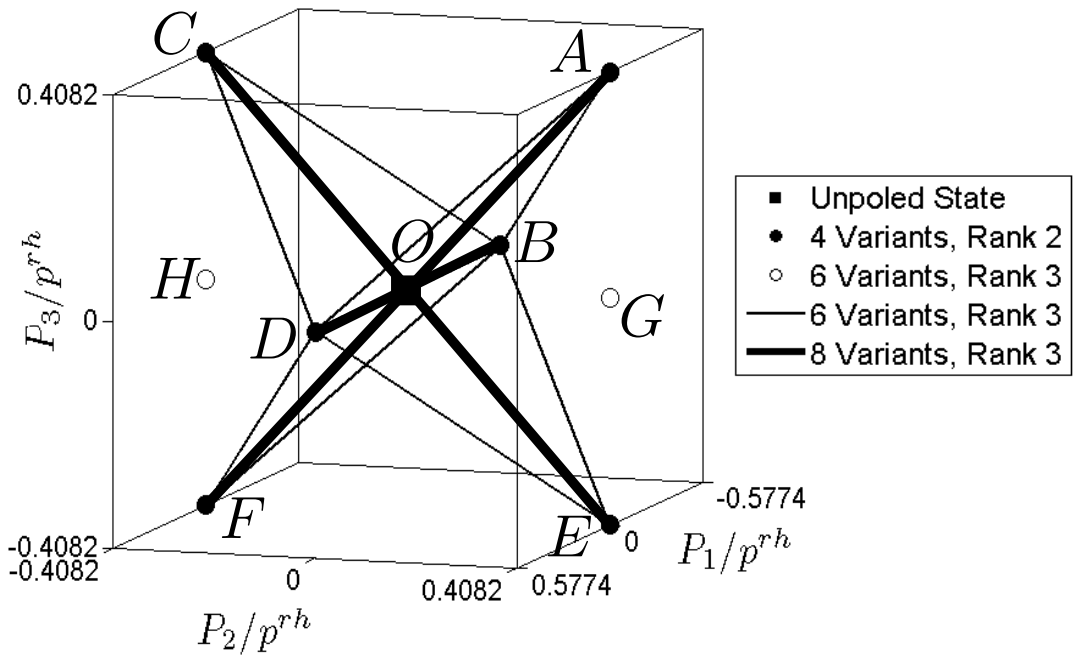

Figure 4.12: The exactly compatible states in the space of possible macroscopic strain and polarization of a rhombohedral $[011]$ film.

evolve continuously between these points, with rank-3 exactly compatible structure and all 8 crystal variants present. There are also 8 distinct lines connecting points A–F, corresponding to rank-3 laminates with only 6 variants present; however, they do not directly connect to the unpoled state O. It is interesting to note the existence of two states that are poled in-plane (G and H) in figure 4.12, but are not connected with any other exactly compatible states. Such states may be difficult to reach in practice because there are no compatible routes approaching them. But they would have advantageous stability once reached.

Figure 4.12 suggests a poling path for $[011]$ oriented rhombohedral films along the line $\overline{OA}$. The corresponding evolution of the domain arrangement is shown in figure 4.13. Figure 4.13(a) shows a possible rank-3 domain arrangement for the unpoled state. Along the path $O \rightarrow A$, the domain interfaces of the lowest rank level in the laminate structure move continuously, reducing the volume fraction of variants 2, 4, 5 and 7. Eventually (figure 4.13(d)) these variants vanish completely, and the laminate reaches its maximally poled state by jumping from rank-3 to rank-2 structure, leaving all the high level domain interfaces unchanged. Expressions

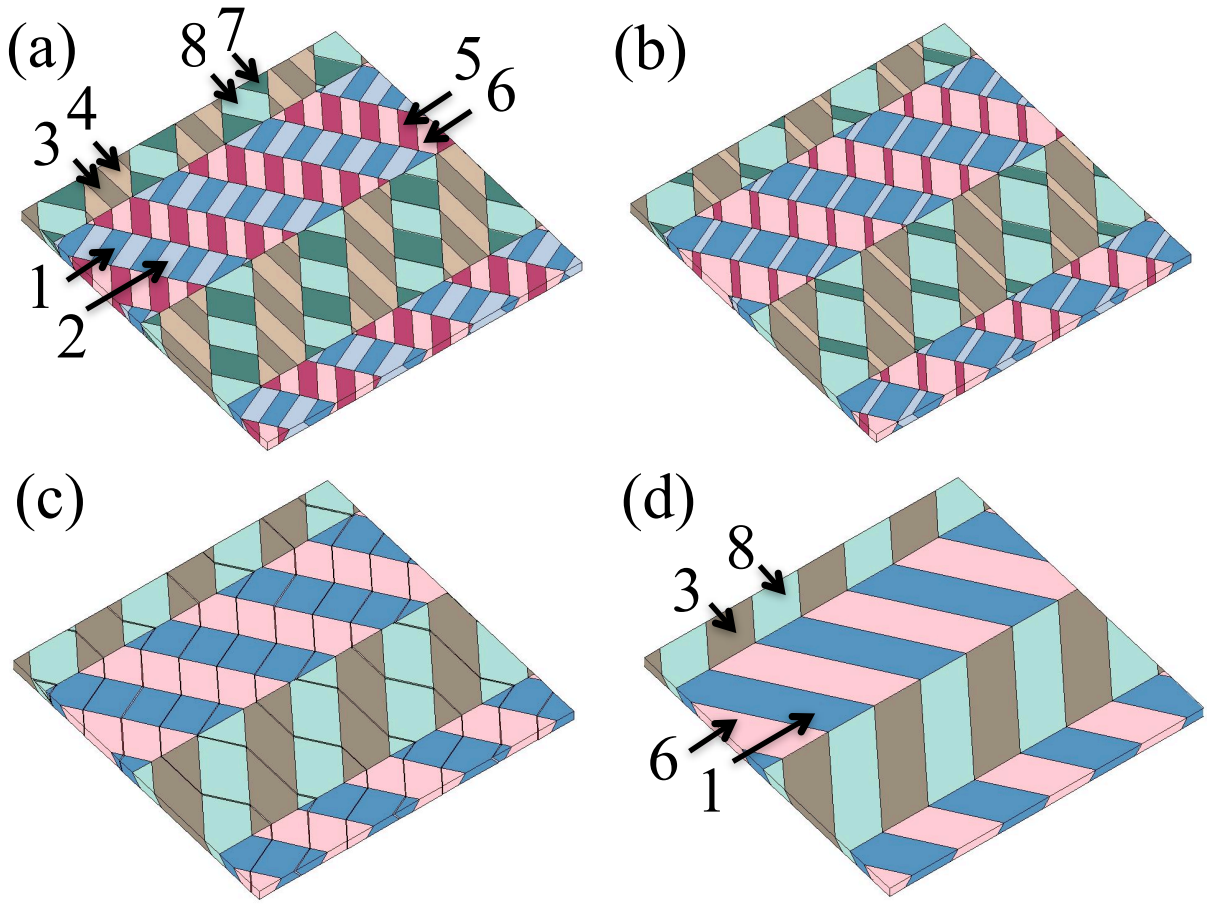

Figure 4.13: The schematic domain evolution along the line $\overline{OA}$ in figure 4.12: (a) unpoled state (b) a typical point on line $\overline{OA}$ (c) as point A is almost reached (d) point A, where the through-thickness polarization P_3 reaches its extremal value.

for the variant composition along $\overline{OA}$, corresponding to the lowest level of the tree diagram, are shown in table 4.12, where the value of x varies in the range ($\frac{1}{8} \leq x \leq \frac{1}{4}$). Note that in the poled state the two variants numbered 6 and 8 contribute nothing to the through-thickness polarization. Their presence is necessary only to ensure that the average strain in the film remains compatible with the substrate. If these two crystal variants were removed, a greater polarization could be achieved by having only variants 1 and 3 present, but this would require in-plane strain ϵ^r_{22} to have the value $-\beta^{rh}$. This suggests that an enhanced polarization could be achieved in $[011]$ rhombohedral films by appropriate compression of the substrate.

Table 4.12: The arrangement of crystal variants and volume fractions on line $\overline{OA}$ in figure 4.12 and figure 4.14 . ($\frac{1}{8} \leq x \leq \frac{1}{4}$)

Node	8	9	10	11	12	13	14	15
Variant	5	6	2	1	4	3	7	8
f_i	$\frac{1}{4} - x$	x	$\frac{1}{4} - x$	x	$\frac{1}{4} - x$	x	$\frac{1}{4} - x$	x

4.4.3 $[111]$ oriented rhombohedral film

In the $[111]$ oriented film, the global macroscopic strain and polarization states are obtained by using equation (4.1). The resulting strain and polarization states are shown in table 4.13. As before, the case of zero in-plane strain is considered, so that $\epsilon^r_{11} = \epsilon^r_{22} = \epsilon^r_{12} = 0$ and $\epsilon^r_{33} = 0$ due to the isochoric nature of remanent straining. This leaves a macroscopic state space of 5 free variables: P_1, P_2, P_3, ϵ^r_{13} and ϵ^r_{23}. Inspection of the ϵ_{11}, ϵ_{22} and ϵ_{12} components in table 4.13 shows that the volume fractions are forced to satisfy $f_{(1)} + f_{(2)} = f_{(3)} + f_{(4)} = f_{(5)} + f_{(6)} = f_{(7)} + f_{(8)} = 1/4$ due to the substrate constraint. It follows that ϵ^r_{13} and ϵ^r_{23} are also forced to be zero, leaving only P_1, P_2 and P_3 as free variables. Furthermore, inspection of the p_3 components, in the context of the constrained volume fractions, indicates that the macroscopic through-thickness polarization P_3 is limited to be no greater than $p^{rh}/2$. Note that this limit follows from equations (2.12)–(2.14) with $f_{(k)} \geq 0$ and does not take account of the exact compatibility requirement.

Figure 4.14 shows the poling map for the $[111]$ rhombohedral film in (P_1, P_2, P_3) space. Points on the edges of the octahedron $ABCFDE$ represent states with exactly compatible laminate structures of rank-3, and 6 crystal variants present. The 6 vertices (A–F) allow rank-2 structures with 4 variants only. Lines $\overline{AF}$, $\overline{BD}$, and $\overline{CE}$ join these vertices and pass through the central, unpoled state, O; the corresponding structures are of rank-3 and have all 8 variants present. It is interesting to compare this poling map with that of the $[011]$ oriented rhombohedral films in figure 4.12. The two maps are related by a pure rotation, and so contain identical points and lines, except that the square $ACFE$ in figure 4.14 does not appear in figure 4.12 because

Table 4.13: Polarization and strain states of the [111] oriented rhombohedral crystal variants in global coordinates.

	Variant Number							
	1	2	3	4	5	6	7	8
p_1/p^{rh}	0	0	$\frac{-1}{\sqrt{3}}-\frac{1}{3}$	$\frac{1}{\sqrt{3}}+\frac{1}{3}$	$-2/3$	$2/3$	$\frac{1}{\sqrt{3}}-\frac{1}{3}$	$\frac{1}{3}-\frac{1}{\sqrt{3}}$
p_2/p^{rh}	0	0	$\frac{1}{\sqrt{3}}-\frac{1}{3}$	$\frac{1}{3}-\frac{1}{\sqrt{3}}$	$-2/3$	$2/3$	$-\frac{1}{\sqrt{3}}-\frac{1}{3}$	$\frac{1}{\sqrt{3}}+\frac{1}{3}$
p_3/p^{rh}	1	-1	$1/3$	$-1/3$	$-1/3$	$1/3$	$1/3$	$-1/3$
ϵ_{11}/β^{rh}	-1	-1	$\frac{1}{3}+\frac{2\sqrt{3}}{3}$	$\frac{1}{3}+\frac{2\sqrt{3}}{3}$	$1/3$	$1/3$	$\frac{1}{3}-\frac{2\sqrt{3}}{3}$	$\frac{1}{3}-\frac{2\sqrt{3}}{3}$
ϵ_{12}/β^{rh}	0	0	$-2/3$	$-2/3$	$4/3$	$4/3$	$-2/3$	$-2/3$
ϵ_{13}/β^{rh}	0	0	$-\frac{1}{\sqrt{3}}-\frac{1}{3}$	$-\frac{1}{\sqrt{3}}-\frac{1}{3}$	$2/3$	$2/3$	$\frac{1}{\sqrt{3}}-\frac{1}{3}$	$\frac{1}{\sqrt{3}}-\frac{1}{3}$
ϵ_{22}/β^{rh}	-1	-1	$\frac{1}{3}-\frac{2\sqrt{3}}{3}$	$\frac{1}{3}-\frac{2\sqrt{3}}{3}$	$1/3$	$1/3$	$\frac{1}{3}+\frac{2\sqrt{3}}{3}$	$\frac{1}{3}+\frac{2\sqrt{3}}{3}$
ϵ_{23}/β^{rh}	0	0	$\frac{1}{\sqrt{3}}-\frac{1}{3}$	$\frac{1}{\sqrt{3}}-\frac{1}{3}$	$2/3$	$2/3$	$-\frac{1}{\sqrt{3}}-\frac{1}{3}$	$-\frac{1}{\sqrt{3}}-\frac{1}{3}$
ϵ_{33}/β^{rh}	2	2	$-2/3$	$-2/3$	$-2/3$	$-2/3$	$-2/3$	$-2/3$

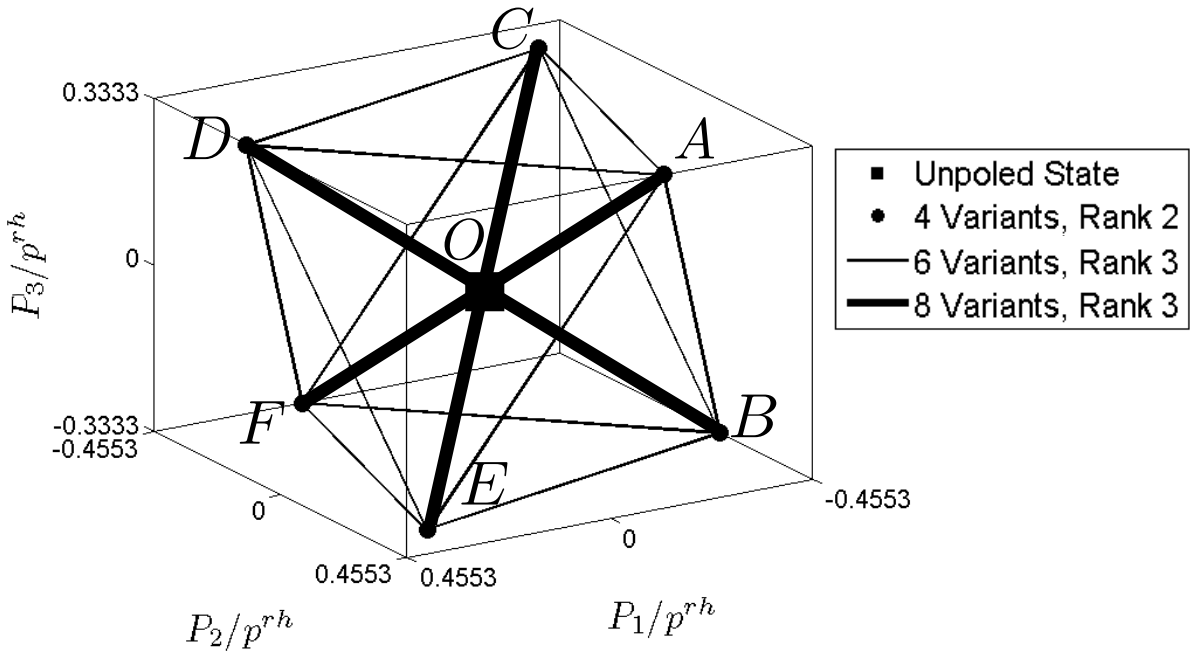

Figure 4.14: The exactly compatible states in the space of possible macroscopic strain and polarization of a rhombohedral [111] film.

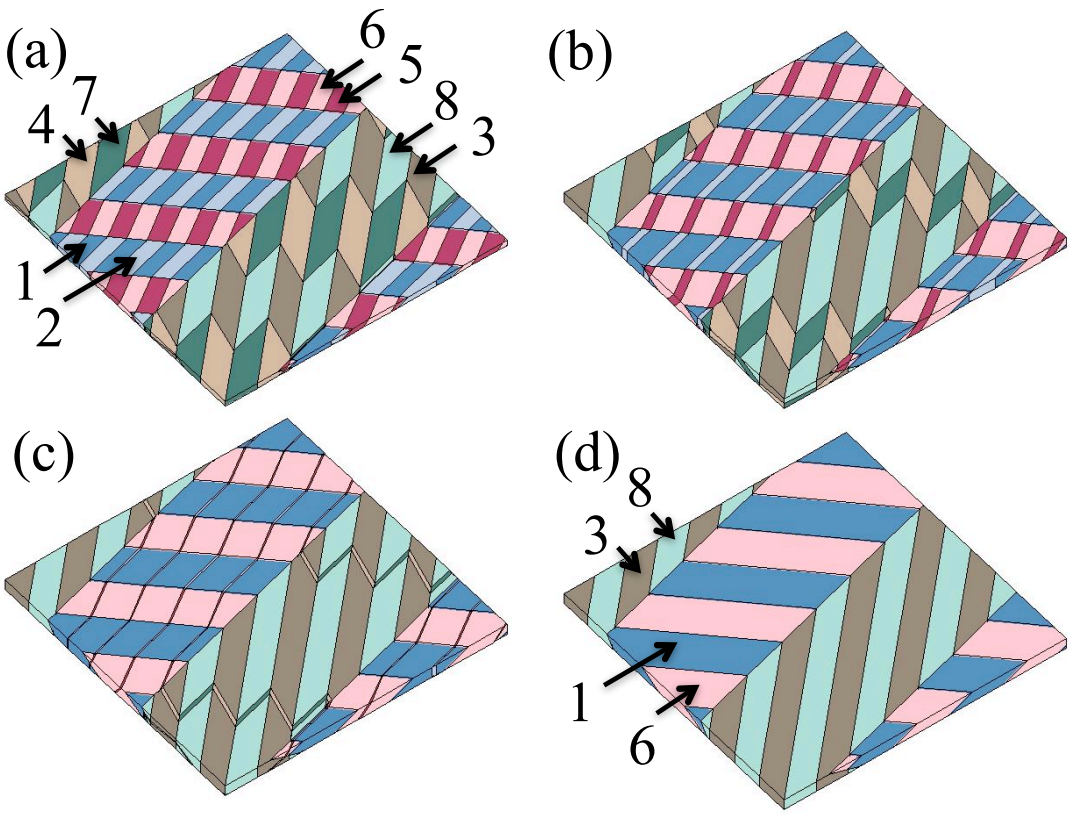

Figure 4.15: The schematic domain evolution along the line $\overline{OA}$ in figure 4.14: (a) unpoled state (b) a typical point on line $\overline{OA}$ (c) as point A is almost reached (d) point A, where the through-thickness polarization P_3 reaches the maximum value the exactly compatible structure can achieve.

these states are prohibited in the $[011]$ film by the constraint that $\mathbf{n}_i \nparallel [001]$.

Figure 4.14 suggests a poling path, line $\overline{OA}$, which connects the unpoled state, O, and a state with the greatest achievable through-thickness polarization for an exactly compatible structure. Note that the maximal P_3 value, reached at point A, is $p^{rh}/3$, which is less than the limit of $p^{rh}/2$ that was found by considering volume fraction constraints alone. In the previous examples of $[001]$ and $[011]$ oriented rhombohedral films, the limiting value of P_3 imposed by considering only volume fraction constraints could be achieved with exactly compatible structure. However, in the $[111]$ film, the limiting value $P_3 = p^{rh}/2$ could only be achieved by averagely compatible laminates with local incompatibilities.

The domain evolution along path $O \to A$ is shown in figure 4.15. This path has identical

domain arrangement to the poling path found for the $[011]$ rhombohedral film. The domain patterns in figures 4.13 and 4.15 are simply two different cross-sections of the same structures. Consequently the set of crystal variants and volume fractions in the lowest level of the tree diagram on the poling path of the $[111]$ film is as shown in table 4.12.

It is worth comparing the results in the present work to those generated by a phase field approach. In the work done by Shu and Yen [84], compatible martensitic domain structures in constrained trigonal films with $[001]$, $[011]$, and $[111]$ orientation are shown. Interestingly, in the cases of $[001]$ and $[011]$ orientation their domain patterns are identical to those in figures 4.11(f) and 4.13(d). However, in $[111]$ oriented films, different results are obtained due to the assumption of laminate domain patterns in the present work.

5

Kinetics approach and applications

5.1 Microstructural evolution and actuation strain

So far the study in chapters 2 to 4 was purely kinematic in nature. The nucleation of new domains and the route along which the microstructure evolves between the identified states were not yet captured. However, these issues are crucial in the design of sensors and actuators because they have significant effects on the hysteresis response and actuation strain output. For example, if new domains cannot form, this would limit the switching ability of a ferroelectric. Thus, it is of interest to study the kinetic behaviour that governs microstructural evolution.

In recent years, polycrystalline lead zirconate titanate (PZT) has been widely used in sensors and actuators. However, the level of actuation strain of PZT is limited (typically less than 0.5%) compared to that of ferroelectric single crystals [4, 23]. For example, relaxor material, lead zirconate niobate and lead titanate (PZN-PT) single crystals can achieve up to 1.7% electrostrictive strain [4]; barium titanate ($BaTiO_3$) single crystals can generate 0.9% actuation strain [28]. Among these materials, $BaTiO_3$ is a lead-free ferroelectric material with a great potential to replace lead based ferroelectrics in the future. It has been extensively studied for decades [1, 24, 28, 108]. Theoretically, a $BaTiO_3$ single crystal can achieve up to 1.09% actuation strain by undergoing a complete 90° tetragonal phase switching [24]. However, such high

actuation strain has not been observed in experiments [62]. This issue has gained much interest and has been broadly discussed recently. Shilo *et al.* [69] suggest this reduction of strain in experiments is due to the friction at the interfaces between the loading frame and crystal surfaces. Models done by Yen *et al.* [64] and Weng and Wong [62] take depolarization energy into account to simulate this behaviour. Shieh *et al.* [109] ascribe this phenomena to the incomplete switching of the crystal at the saturation state, leaving some domains with antiparallel polarization. Such a domain arrangement can result in a "polarization-free" strain change when the direction of applied electric field is reversed. Although different explanations are given by these studies, they all suggest one thing in common: the actuation strain of the ferroelectric single crystal is largely dependent on the applied electromechanical loads, induced domain switching and the evolution of domain structure.

In this chapter, a general theory of kinetics based on a conventional kinetic model [61,63] is used, to model the behaviour of microstructures in a ferroelectric single crystal with laminate domain patterns. Then, the theory is applied to study the relationship between domain patterns and hysteresis responses in barium titanate single crystals in the tetragonal crystal system. As many domain patterns of rank-2 or lower are commonly observed in experiments and found as minimum energy solutions in phase field models [1, 11], here we only focus on the laminate domain pattern of rank-2 or lower; all the microstructures considered in this chapter are periodic and satisfy compatibility equations across every domain wall. However, the model is suitable for domain patterns of higher rank, other crystal systems or related materials such as shape memory alloys.

5.2 Kinetic model for laminate domain structures

5.2.1 Theory

Consider a ferroelectric single crystal containing domains and domain walls, subjected to a given kinetic or dissipative process. As mentioned in equation (1.5) in chapter 1, the system can be described by a variational functional

$$\Pi = \dot{G} + \Psi \tag{5.1}$$

where $\dot{G}$ is the rate of change of Gibbs free energy, and Ψ is a rate potential arising due to the dissipative nature of domain evolution. The Gibbs free energy is the sum of the internal energy U and potential energy Ω, i.e. $G = U + \Omega$. For simplicity, the energy stored in the free space external to the region of interest and the domain wall energy itself are neglected in the present analysis. These energies are typically small provided that the ferroelectric has high relative permittivity compared to its surrounding, and the domain wall spacing is much larger than the wall thickness. The total internal energy U is associated with elastic energy and electrical energy, and can be written in the form:

$$U = \frac{1}{2}\int_V \epsilon_p^L c_{pq} \epsilon_q^L \mathrm{d}V + \frac{1}{2}\int_V E_k \kappa_{kl} E_l \mathrm{d}V \qquad p,q = 1...6, \quad k,l = 1...3 \tag{5.2}$$

where V is the volume of material we considered; ϵ_p^L is the linear elastic and piezoelectric strain due to the external loads; c_{pq} is the stiffness matrix and κ_{kl} is the permittivity matrix under constant strain; E_k is the electric field. Here, the reduced indicial notation for stress, strain and the elastic constants [97] is used. It is worth noting that the matrices of material properties, such as c_{pq} and κ_{kl}, are different from domain to domain due to the varying crystallographic orientation. Next consider the crystal subjected to a electric potential ϕ, such that $E_i = -\phi_{,i}$

and a surface traction t_i. The potential energy of the applied loads, Ω, is given by

$$\Omega = \int_s (\phi q - t_i u_i) \mathrm{d}s = \int_V (-E_k D_k - \sigma_p \epsilon_p) \mathrm{d}V \tag{5.3}$$

where q is the surface charge density; u_i is the surface displacement; D_k and ϵ_p are the electric displacement and strain of each material point, respectively. They can be determined by

$$\begin{aligned} D_k &= D_k^L + P_k = d_{kp}\sigma_p + \kappa_{kl}^{\sigma} E_l + P_k \\ \epsilon_p &= \epsilon_p^L + \epsilon_p^r = s_{pq}\sigma_q + d_{kp}E_k + \epsilon_p^r \end{aligned} \tag{5.4}$$

Here, s_{pq} is the compliance matrix; d_{kp} are matrices of piezoelectric coefficients; κ_{kl}^{σ} is the permittivity matrix under constant stress; P_k and ϵ_p^r are the remanent polarization and strain states, respectively. The rate potential Ψ is associated with the movement of all the domain walls present in the region of interest. Here linear kinetics is used such that Ψ is quadratic in domain wall velocity. Then, the total rate potential Ψ is the summation of the rate potential $\Psi_{(W)}$ for each domain wall W, given by

$$\Psi = \sum \Psi_{(W)} = \sum \frac{1}{2} \int_{A_{(W)}} \frac{1}{m_{(W)}} v_{(W)}^2 \mathrm{d}A_{(W)} \tag{5.5}$$

where $m_{(W)}$ is the domain wall mobility; $A_{(W)}$ and $v_{(W)}$ are the area and velocity of domain wall W, respectively. For simplicity, we set the same value of mobility m for all domain walls in the current work.

It has been shown that the kinetic system evolves along a path which makes the functional Π stationary with respect to the domain wall velocity $v_{(W)}$ [68], that is:

$$\frac{\partial \Psi}{\partial v_{(W)}} = -\frac{\partial \dot{G}}{\partial v_{(W)}} \tag{5.6}$$

The domain wall velocities $v_{(W)}$ can be obtained directly by solving equation (5.6); the path of domain evolution can then be found.

5.2.2 Unit cells of periodic multi-rank laminate domain patterns

In this work, we study periodic multi-rank laminate domain patterns which satisfy the compatibility equations across every domain wall. A periodic domain structure can be represented as unit cell containing domains and domain walls. The position of a domain wall is described by a dimensionless variable a_r within the range $0 \leq a_r \leq 1$. In order to maintain a laminated structure, assume that the domain walls in the unit cell of the periodic laminate are planar and can only move along the direction of the domain interface normal. Note that the positions of the set of domain walls, which are represented by nodes in the same level of the tree diagram, are described by exactly one degree of freedom since these domain walls need to move equal amounts to maintain the compatibility between domains throughout. Thus, there are R degrees of freedom for a rank-R compatible laminate domain pattern, and degree of freedom a_r specifies the position of the domain walls which are represented by the nodes in the rth level of the tree diagram. To illustrate this, take the rank-2 domain pattern "5354" as an example. Figure 5.1(a) shows the unit cell of domain pattern "5354" containing two types of domain walls. Define a unit cell in the form of a cube with volume $V = L^3$. The positions of the domain walls can be described by two degrees of freedom a_1 and a_2. The domain walls divide the unit cell into several regions, labelled A to D. The regions A to D contain crystal variants 5, 3, 5 and 4 respectively. The total volumes of these four regions $V^{(A)}$ to $V^{(D)}$ can then be determined: $a_1 a_2 L^3$, $a_2(1-a_1)L^3$, $a_1(1-a_2)L^3$ and $(1-a_1)(1-a_2)L^3$.

Domain switching can be achieved by changing the domain wall positions a_1 and a_2. For example, let the domain wall between variants 5 and 3 move, so as to increase the volume fraction of variant 5 (region A in figure 5.1). Then, the corresponding domain wall between variants 5 and 4 (regions C and D) must also move in order to maintain compatibility. Thus

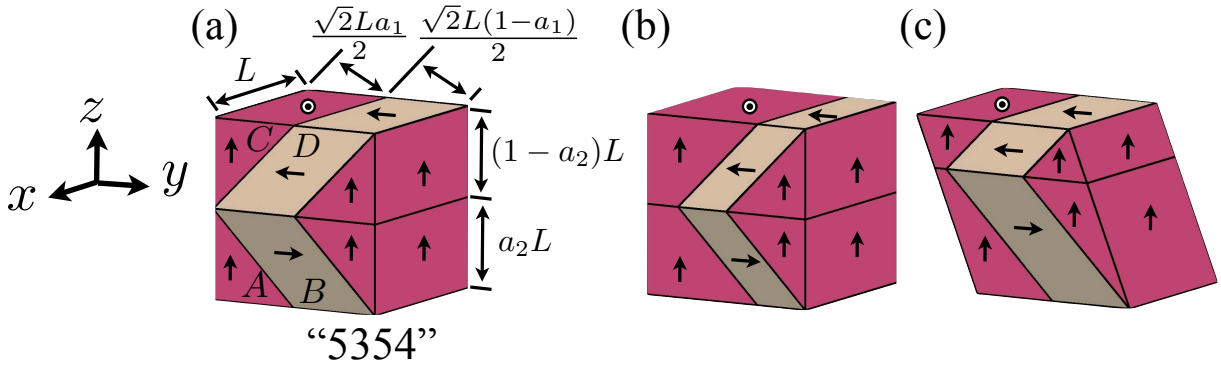

Figure 5.1: (a) A unit cell of domain pattern "5354" with two types of domain wall controlled by degrees of freedom a_1 and a_2. (b) Movement of the a_1 domain wall maintains the volume and shape of the unit cell. (c) Movement of the a_2 domain wall distorts the unit cell.

variants 3 and 4 shrink as variant 5 grows. This change corresponds to the degree of freedom a_1 as shown in figure 5.1(b). Note that the topology remains as "5354"; only the volume fractions of crystal variants have changed. In the limit where variants 3 and 4 disappear altogether, $a_1 = 1$, leaving a pure single domain of variant 5 (a rank-0 structure). The lower rank laminates that can form as limiting cases of each higher rank laminate may be viewed as "pivot states" that allow transition between different domain structures. This will be discussed in more detail in section 5.3. Conversely, if variants 3 and 4 grow, a state can be reached where variant 5 has vanished, i.e. $a_1 = 0$, the structure then becomes a rank-1 lamination "34". The microstructure has then switched from rank-2 to rank-1. Note that the changes of the degree of freedom a_1 do not alter the unit cell shape or volume. In contrast, consider a change of the degree of freedom a_2. This distorts the unit cell, as shown in figure 5.1(c), in order to maintain compatibility between every adjacent domain. Note carefully that the distortion shown in figure 5.1(c) is a change of the pattern of domain walls, but does not represent deformation of the material itself. This results in long-range non-periodic domain wall displacements over the crystal. Such long range domain wall motions are effectively pinned because they are associated with a high degree of dissipation. Therefore, the a_2 domain wall in this periodic pattern is effectively locked and only the a_1 domain walls are mobile. This constraint on the degree of freedom a_2 becomes unlocked when a_1 reaches either 1 or 0. In these limits, changes of a_2 do not change the unit

cell shape. Note that, by contrast, the domain walls associated with degree of freedom a_1 are always mobile, regardless of the value of a_2.

5.2.3 Locking of domain patterns

To model this locking effect, the degree of freedom a_r, which specifies the position of the domain wall represented by the nodes in the rth level of a given tree diagram, is mobile if and only if its change does not affect the volume or shape of the unit cell. Equivalently, all the 'present domain walls' in the same level j of the tree diagram (where $j = 1 \dots r-1$) in contact with the domain wall interfaces controlled by a_r are parallel. Here a 'present domain wall' is defined as a domain wall which is not eliminated by any related degree of freedom reaching its extremal values (0 or 1).

This can be illustrated by an example of a complex rank-4 domain pattern as shown in figure 5.2(a). The position of domain walls in the pattern is controlled by $a_r l_r$ ($1 \geq a_r \geq 0$, $r = 1 \dots 4$), where l_r is the assigned length scale of the domain wall spacing of rth rank. The corresponding tree diagram shown in figure 5.2(c) reveals the relationship between domain wall normals; however, nodes in the bottom level of the tree are neglected as they represent pure crystal variants and have no information about domain walls. Now consider whether the a_3 domain walls are mobile or sessile. The a_3 domain walls are mobile when

$$\begin{aligned}
&\|\mathbf{n}_4 \times \mathbf{n}_5\| a_4 a_2 (1-a_2) + \\
&\|\mathbf{n}_6 \times \mathbf{n}_7\| (1-a_4) a_2 (1-a_2) + \\
&\|\mathbf{n}_8 \times \mathbf{n}_{10}\| a_4 a_2 a_1 (1-a_1) + \|\mathbf{n}_{12} \times \mathbf{n}_{14}\| (1-a_4) a_2 a_1 (1-a_1) + \\
&\|\mathbf{n}_9 \times \mathbf{n}_{11}\| a_4 (1-a_2) a_1 (1-a_1) + \|\mathbf{n}_{13} \times \mathbf{n}_{15}\| (1-a_4)(1-a_2) a_1 (1-a_1) = 0
\end{aligned} \tag{5.7}$$

where $\|\mathbf{n}_p \times \mathbf{n}_q\|$ is the norm of the cross product of $\mathbf{n}_p$ and $\mathbf{n}_q$, and it is zero when $\mathbf{n}_p \parallel \mathbf{n}_q$. The first row of equation (5.7) means that the domain walls associated with $\mathbf{n}_4,\ \mathbf{n}_5$ do not lock the a_3 domains if $\mathbf{n}_4 \parallel \mathbf{n}_5$ or if they are not present in the pattern, i.e. $a_4 = 0$ or a_2 reaches its

limit. The second row of equation (5.7) indicates that the domain walls of $\mathbf{n}_6,\ \mathbf{n}_7$ do not lock the a_3 domains if $\mathbf{n}_6 \parallel \mathbf{n}_7$ or if they are not present, i.e. $a_4 = 1$ or a_2 reaches its limit. Similar requirements for domain wall normals $\mathbf{n}_8 \ldots \mathbf{n}_{15}$ are also introduced in the third and fourth rows in equation (5.7). Next consider this domain pattern in a limiting state where $a_2 = 0$ as an example. This rank-4 laminate then reduces into a rank-3 laminate as shown in figure 5.2(b), where the domain walls marked by dashed lines represent the vanished domain walls associated with $\mathbf{n}_4$, $\mathbf{n}_5$, $\mathbf{n}_6$ and $\mathbf{n}_7$. The left hand side of equation (5.7) is then simplified to

$$\|\mathbf{n}_9 \times \mathbf{n}_{11}\| a_4 a_1 (1 - a_1) + \|\mathbf{n}_{13} \times \mathbf{n}_{15}\| (1 - a_4) a_1 (1 - a_1) \tag{5.8}$$

In this example, the domain pattern has $\mathbf{n}_9 \parallel \mathbf{n}_{11}$ and $\mathbf{n}_{13} \parallel \mathbf{n}_{15}$ which makes equation (5.8) equal to zero. Thus, the degree of freedom a_3 is mobile in the configuration shown in figure 5.2(b).

Here an algorithm to identify in general cases whether the domain wall is mobile or sessile by examining the corresponding tree diagram is provided. The tree diagram of a rank-R domain pattern contains $2^{R+1} - 1$ nodes, in which node numbers $1 \ldots 2^R - 1$ are associated with interface normals. The degree of freedom a_r is mobile when

$$\sum_{i=2^{R-r}}^{2^{R-r+1}-1} \sum_{j=1}^{r-1} \sum_{k=1}^{2^{j-1}} a_l (1 - a_l) \|\mathbf{n}_p \times \mathbf{n}_q\| \prod_{x=1}^{R-l} C = 0 \tag{5.9}$$

where $p = 2^j i + k - 1$; $q = p + 2^{j-1}$; $l = R - \lfloor \log_2 p \rfloor$; and

$$C = \begin{cases} 1, & \text{when } x = r - l \\ (1 - 2b) a_{x+l} + b, & \text{otherwise.} \end{cases} \tag{5.10}$$

where

$$b = \left\lfloor \frac{p - 2^{R-l}}{2^{x-1}} \right\rfloor - 2 \left\lfloor \frac{p - 2^{R-l}}{2^x} \right\rfloor \tag{5.11}$$

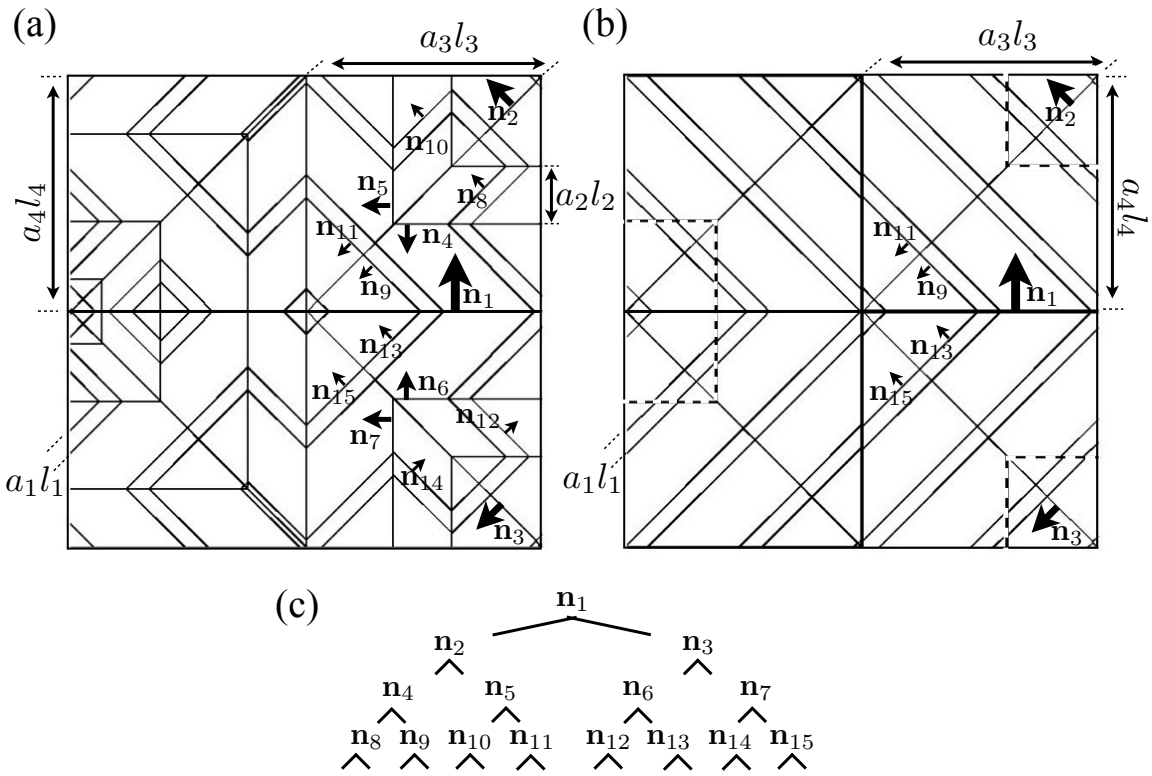

Figure 5.2: (a) A schematic rank-4 domain pattern with 4 degrees of freedom $a_1 \dots a_4$, and (b) the domain pattern with the a_2 domain walls reaching their extremal position ($a_2 = 0$). (c) The corresponding tree diagram showing the relationship between domain wall normals.

If the condition shown in equation (5.9) is not satisfied, the degree of freedom a_r is sessile. For example, the mobility of a_2 domains in pattern "5354" is considered. We substitute $r = 2$ into equation (5.9), and the left hand side of equation (5.9) becomes

$$a_1(1 - a_1)\|\mathbf{n}_2 \times \mathbf{n}_3\| \tag{5.12}$$

where $\mathbf{n}_2 = [0, 1, 1]$ and $\mathbf{n}_3 = [0, -1, 1]$. Clearly, this only equals zero when $a_1 = 1$ or 0. Thus, as expected, the a_2 domain in pattern "5354" is sessile unless $a_1 = 1$ or 0. In this way, sufficient information for studying the domain evolution in compatible laminate structures, including the arrangement of domains, domain wall mobility and the volume fractions of the contained crystal variants, can be obtained. We are now ready to apply the kinetic theory to multi-rank laminate patterns.

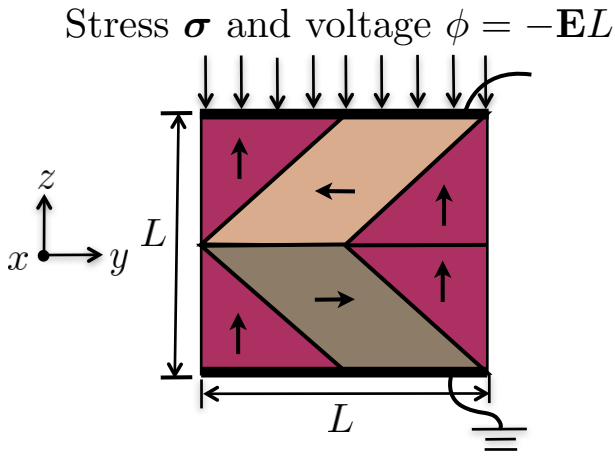

Figure 5.3: The crystal containing domain pattern "5354" is subjected to a cyclic electric field parallel to the z-axis combined with a constant compressive uniaxial stress along the z-axis.

5.2.4 Application to rank-2 laminates

The variational model is now applied to predict the hysteresis response of a ferroelectric crystal with domain pattern "5354" as shown in figure 5.1(a). In this section, the crystal is assumed to contain a specific domain pattern without considering the possibility of switching between different domain patterns. The crystal is subjected to a cyclic electric field parallel to the z-axis combined with a constant compressive uniaxial stress along the z-axis, as shown in figure 5.3. This loading system is motivated by the experiments of Burcsu *et al.* [28]. Next the overall internal energy U and potential energy Ω are calculated using equations (5.2)–(5.4). Uniform stress and electric field are assumed throughout the crystal, i.e. the Reuss approximation [110]. Thus each domain is subjected to the applied electric field and stress. This type of approximation is commonly used in ferroelectric modelling [30–32, 66]. Thus, the internal energy U in equation (5.2) can now be expressed as

$$\begin{aligned} U &= \tfrac{1}{2}\textstyle\int_V (s_{ps}\sigma_s + d_{kp}E_k)c_{pq}(s_{qs}\sigma_s + d_{lq}E_l)\mathrm{d}V + \tfrac{1}{2}E_kE_l\textstyle\int_V \kappa_{kl}\mathrm{d}V \\ &= \tfrac{1}{2}\textstyle\int_V \left[\sigma_p s_{pq}\sigma_q + E_kE_l(\kappa_{kl} + d_{kp}c_{pq}d_{lq}) + 2d_{kp}E_k\sigma_p\right]\mathrm{d}V \end{aligned} \tag{5.13}$$

Note that the piezoelectric coefficient $e_{kq} = d_{kp}c_{pq}$, and the permittivity under constant stress $\kappa^{\sigma}_{kl} = \kappa_{kl} + e_{kq}d_{lq}$. Therefore, equation (5.13) can be simplified further to

$$\begin{aligned} U &= \tfrac{1}{2}\sigma_p\sigma_q \textstyle\int_V s_{pq}\mathrm{d}V + \tfrac{1}{2}E_kE_l \textstyle\int_V \kappa^{\sigma}_{kl}\mathrm{d}V + E_k\sigma_p \textstyle\int_V d_{kp}\mathrm{d}V \\ &= \tfrac{1}{2}\sigma_p\bar{s}_{pq}\sigma_q + \tfrac{1}{2}E_k\bar{\kappa}^{\sigma}_{kl}E_l + E_k\bar{d}_{kp}\sigma_p \end{aligned} \tag{5.14}$$

where $\bar{s}_{pq},\ \bar{\kappa}^{\sigma}_{kl},\ \bar{d}_{kp}$ denote the effective compliance, permittivity under stress and piezoelectric coefficient, respectively. Similarly, equation (5.3) can be simplified to

$$\begin{aligned} \Omega &= -E_k \textstyle\int_V (d_{kp}\sigma_p + \kappa^{\sigma}_{kl}E_l + P_k)\mathrm{d}V - \sigma_p \textstyle\int_V (s_{pq}\sigma_q + d_{kp}E_k + \epsilon^r_p)\mathrm{d}V \\ &= -E_kE_l \textstyle\int_V \kappa^{\sigma}_{kl}\mathrm{d}V - \sigma_p\sigma_q \textstyle\int_V s_{pq}\mathrm{d}V - 2E_k\sigma_p \textstyle\int_V d_{kp}\mathrm{d}V - E_k \textstyle\int_V P_k\mathrm{d}V - \sigma_p \textstyle\int_V \epsilon^r_p\mathrm{d}V \\ &= -E_k\bar{\kappa}^{\sigma}_{kl}E_l - \sigma_p\bar{s}_{pq}\sigma_q - 2E_k\bar{d}_{kp}\sigma_p - E_k\overline{P_k} - \sigma_p\overline{\epsilon^r_p} \end{aligned} \tag{5.15}$$

where $\overline{P_k}$ and $\overline{\epsilon^r_p}$ are the effective remanent polarization and strain. In laminate structures, we can obtain these effective properties by volume averaging the local properties of crystal variants present in the crystal. Note that the resulting effective properties are dependent on the volume fraction of each domain type. Thus, according to equations (5.2)–(5.4), the internal energy and potential energy are functions of the domain wall position, applied stress and electric field, i.e. $U(a_r, \boldsymbol{\sigma}, \mathbf{E})$ and $\Omega(a_r, \boldsymbol{\sigma}, \mathbf{E})$. The assumption of uniform stress and electric field throughout the crystal here will be validated by the finite element analysis later on.

Next, the total rate potential $\Psi = \Psi(a_j, \dot{a_k})$ is a function of the domain wall positions and velocities. There are two types of domain wall in the unit cell of domain pattern "5354": domain wall (1) are 90° domain walls controlled by a_1; domain wall (2) is the domain wall controlled by a_2 as shown in figure 5.1(a). Domain walls (1) and (2) have total area $A_{(1)} = \sqrt{2}L^2$ and $A_{(2)} = L^2$ in the unit cell, respectively. The velocity of domain wall $V_{(r)}$ is defined as $\dot{a}_r l_r$, where l_r is the length scale of domain spacing, i.e. the total distance moved by the domain wall from $a_r = 0$ to 1. According to equation (5.5), we can determine the total rate potential Ψ of

the "5354" domain pattern which can be given in the form of a_1 and a_2

$$\begin{aligned} \Psi_{5354} &= \tfrac{1}{2m}V_{(1)}^2 A_{(1)} + \tfrac{1}{2m}V_{(2)}^2 A_{(2)} \\ &= \tfrac{1}{2m}\left[(\tfrac{\sqrt{2}L}{2}\dot{a}_1)^2(\tfrac{\sqrt{2}L^2}{2}) + (\tfrac{\sqrt{2}L}{2}\dot{a}_1)^2(\tfrac{\sqrt{2}L^2}{2})\right] + \tfrac{1}{2m}(\dot{a}_2 L)^2 L^2 \\ &= \tfrac{L^4}{2m}(\tfrac{\sqrt{2}}{2}\dot{a_1}^2 + \dot{a_2}^2) \end{aligned} \tag{5.16}$$

where the terms in square brackets indicate that domain wall (1) contains two segments which are not parallel, each having area $\sqrt{2}L^2/2$ and velocity $\frac{\sqrt{2}L}{2}\dot{a}_1$.

It is worth noting that Ψ, G and domain wall velocities $v_{(W)}$ in equation (5.6) can be written in terms of a_1 and a_2. Also, $G = G(a_1, a_2, \boldsymbol{\sigma}, \mathbf{E})$ is a function of configuration and loading only, but is independent of the rate $\dot{a}_r$. Therefore, we can rewrite equation (5.6) as

$$\frac{\partial \Psi}{\partial \dot{a}_r} = -\frac{\partial G}{\partial a_r} \tag{5.17}$$

where $\frac{\partial G}{\partial a_r}$ can be approximated numerically by giving a small change $\mathrm{d}a_r$ to degree of freedom a_r,

$$\frac{\partial G}{\partial a_r} \approx \frac{G(a_r + \mathrm{d}a_r, \boldsymbol{\sigma}, \mathbf{E}) - G(a_r - \mathrm{d}a_r, \boldsymbol{\sigma}, \mathbf{E})}{2\mathrm{d}a_r}. \tag{5.18}$$

For the domain pattern "5354", equation (5.17) can be written in matrix form

$$\begin{bmatrix} \frac{\sqrt{2}}{2m}L^4 & 0 \\ 0 & \frac{1}{m}L^4 \end{bmatrix} \begin{bmatrix} \dot{a}_1 \\ \dot{a}_2 \end{bmatrix} = - \begin{bmatrix} \frac{\partial G}{\partial a_1} \\ \frac{\partial G}{\partial a_2} \end{bmatrix} \tag{5.19}$$

The rate of change of degrees of freedom at the current time t can then be obtained directly by inverting the 2×2 mobility matrix. Thus, the degree of freedom for the next time step a_r' can be calculated, such that $a_r' = a_r + \dot{a}_r \mathrm{d}t$, where $\mathrm{d}t$ is the time step. Note that, during the calculation, if a_r' violates the condition $1 \geq a_r' \geq 0$, the changes of the degree of freedom at the current time will be ignored, i.e. $a_r' = a_r$. Moreover, as mentioned in section 5.2.2, the a_2 domain wall in domain pattern "5354" is sessile and can become moveable only when a_1 is either 1 or 0. Thus,

Table 5.1: The material parameters of tetragonal single crystal barium titanate used in the present simulation [111].

c_{11}	275×10^9 Pa	c_{12}	179×10^9 Pa	c_{13}	152×10^9 Pa
c_{33}	165×10^9 Pa	c_{44}	54.3×10^9 Pa	c_{66}	113×10^9 Pa
e_{15}	21.3 Cm^{-2}	e_{31}	-2.69 Cm^{-2}	e_{33}	3.65 Cm^{-2}
κ_{11}	1.74×10^{-8} Fm^{-1}	κ_{33}	9.65×10^{-10} Fm^{-1}		

$\dot{a}_2$ remains zero until this case is reached.

In the present work, we study the electromechanical behaviour of single crystal barium titanate with material parameters as shown in table 5.1 [111]. These properties correspond to crystal variant "5" with polarization along the direction of the $+z$-axis. Material properties of the remaining crystal variants can be determined from pure rotation by 90° or 180° according to their orientation. The values of remnant polarization $P_k^{(5)}$ and strain states $\epsilon_p^{r(5)}$ of crystal variant 5 used in this study are given by

$$\begin{aligned} P_k^{(5)} &= \begin{bmatrix} 0, & 0, & 0.26 \end{bmatrix}^{\mathrm{T}} \ \mathrm{Cm}^{-2}, \\ \epsilon_p^{r(5)} &= \begin{bmatrix} -0.42, & -0.42, & 0.67, & 0, & 0, & 0 \end{bmatrix}^{\mathrm{T}} \ \% \end{aligned} \tag{5.20}$$

from the data of Shu and Bhattacharya [24]. Similarly, the remnant polarization and strain states of the other crystal variants can be obtained from pure rotation of those in equation (5.20).

At this stage, we are ready to model the evolution of the "5354" domain pattern under a cyclic electric field parallel to the z-axis combined with a constant compressive uniaxial stress along the z-axis. To match the values used in the experiment of Burcsu *et al.* [28], the applied electric field is $E_3(t) = E_0 \sin(2\pi t)$ with amplitude $E_0 = 1\mathrm{MVm}^{-1}$; the applied stress is $\sigma_3 = -1.78$ MPa. The coercive field is not specified directly in this model. The mobility constant m has been chosen to give domain pattern "5354" a coercive field of about $0.1\mathrm{MVm}^{-1}$.

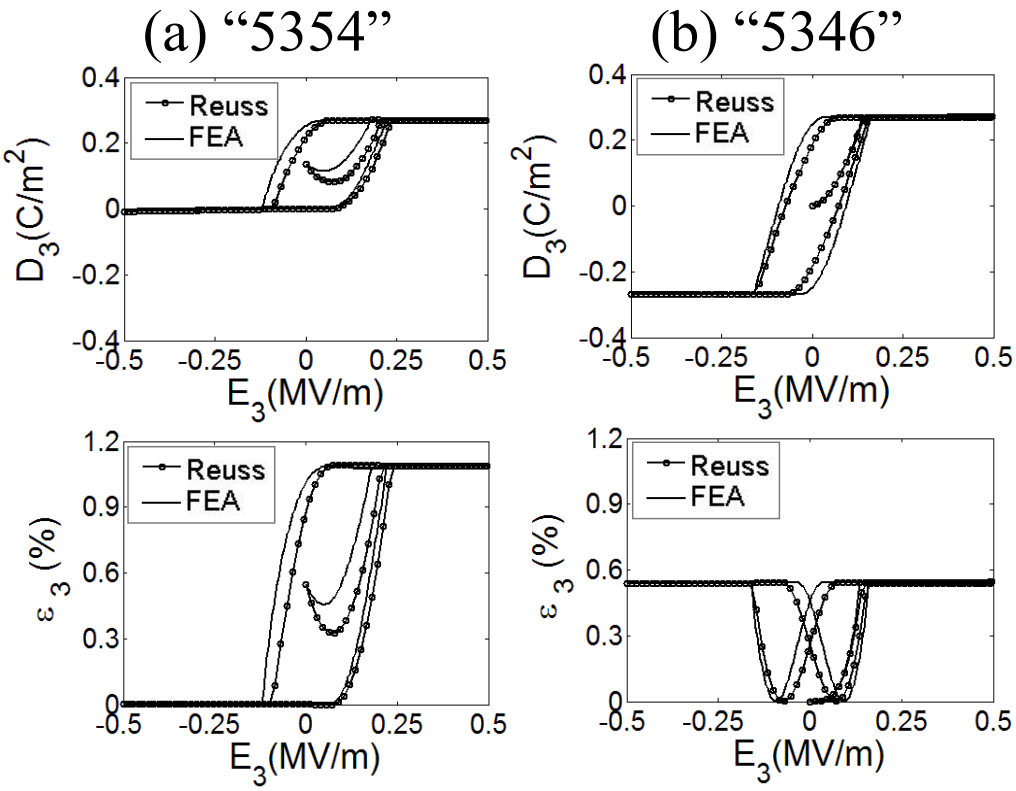

Figure 5.4: Hysteresis responses of domain patterns (a) “5354” and (b) “5346” under a uniform compressive stress $\sigma_3 = -1.78$ MPa and a cyclic electric field along z-direction. The data of the hysteresis response are simulated by the present model with Reuss approximation (Reuss) and finite element analysis (FEA).

The macroscopic electric displacement D_3 and strain ϵ_3 are given by using the formation of equation (5.4) and replacing the corresponding terms by the set of effective properties and volume averaged remnant polarization and strain states.

The initial state of the domain pattern is set to $a_1 = a_2 = 1/2$. This gives a state with equal volume fractions for all four regions. The calculation starts from time $t = 0$ and the time step is set as $\mathrm{d}t = \frac{1}{10000}$ s. For each time step, $\frac{\partial G}{\partial a_r}$ is first determined numerically by using equation (5.18) with $\mathrm{d}a_r = 0.001$. Next, the rate of change of each degree of freedom can be obtained by equation (5.19); degree of freedom a_r, macroscopic electric displacement D_k and strain state ϵ_p for the next time step can then be determined. In this way, the dielectric hysteresis and butterfly hysteresis for domain pattern “5354” can be generated, as shown by lines marked with dots in figure 5.4(a). The electric field axis is limited to $\pm 0.5 \mathrm{MVm}^{-1}$ as all the curves

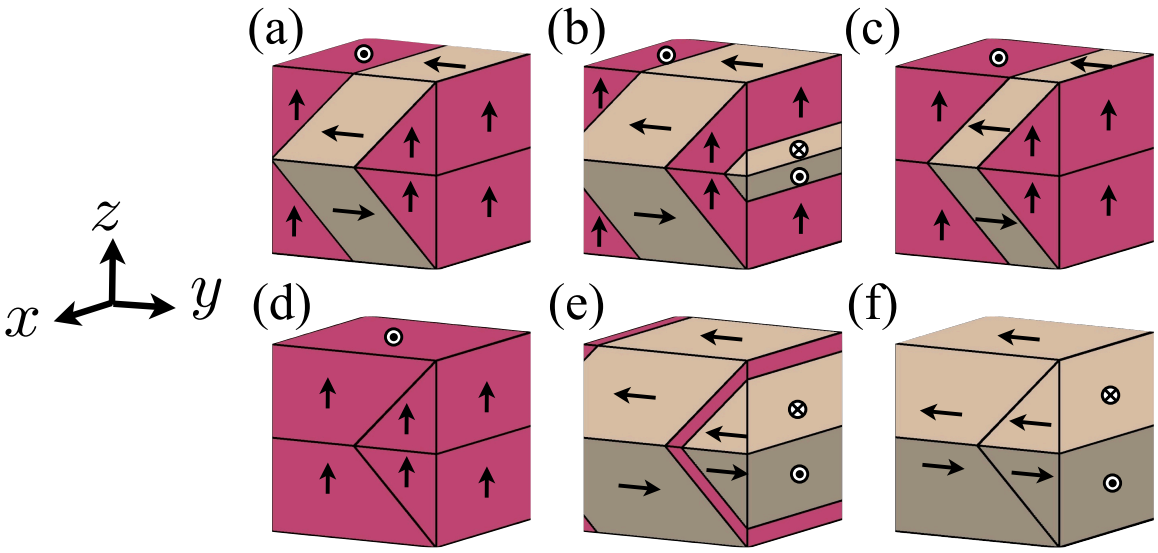

Figure 5.5: The schematic domain evolution for pattern "5354" in the electric loading cycle under stress $\sigma_3 = -1.78\text{MPa}$. (a) The initial state. (b) the compressive loads increase the volume fraction of variants 3 and 4 until the electric field E_3 becomes sufficiently strong. (c) E_3 gradually shrinks the regions containing variants 3 and 4. (d) Single domain state "5". (e) When $E_3 < 0$, the boundary conditions reduce the volume fraction of crystal variant 5, leaving (f) pattern "34".

reach saturation within this range. For later comparison with experiments, the minimum strain point of each butterfly hysteresis loop has been set as a datum of zero strain.

The simulation shows asymmetric dielectric and strain hysteresis loops for domain pattern "5354"; the domain pattern evolution is shown in figure 5.5. Firstly, the compressive stress favours variants 3 and 4, resulting in the growth of the corresponding domain regions (figure 5.5(a)→(b)). However, when the electric field E_3 becomes sufficiently strong, the domain regions with variant 5 start growing and regions 3 and 4 shrink until they vanish (figure 5.5(c)). Thus, a single domain state "5" is reached and remains until $E_3 < 0$ (figure 5.5(d)). At this stage, the symmetry of the compressive loading favours crystal variants 3 and 4 again and reduces the volume fraction of crystal variant 5, leaving "34", a rank-1 laminate of $180°$ domains (figure 5.5(e)→(f)). In addition, since we model only this specific domain pattern, which contains no crystal variant 6, this structure does not evolve further as the electric field becomes more negative and the macroscopic electric displacement saturated at $D_3 = 0\ \text{Cm}^{-2}$. The result

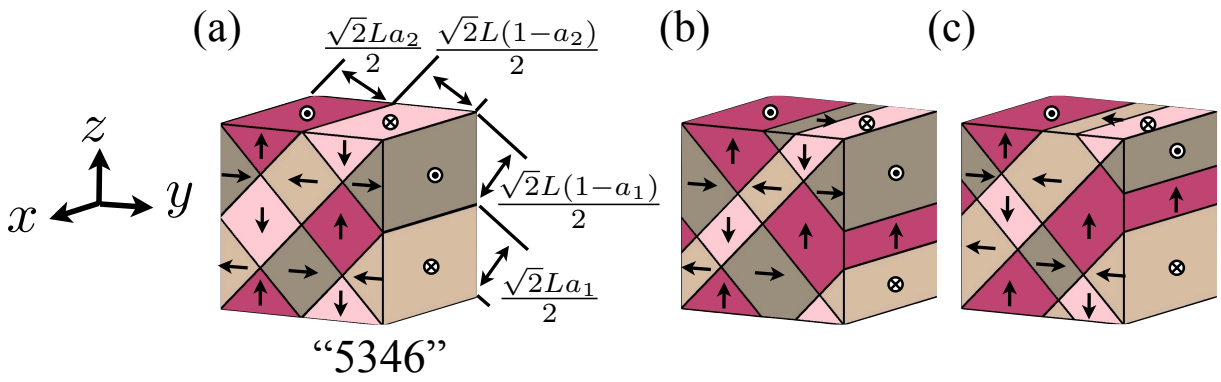

Figure 5.6: (a) A unit cell of domain pattern "5346" with two types of domain wall controlled by degrees of freedom a_1 and a_2. (b) and (c) show both types of movement of the a_1 and a_2 domain walls maintain the volume and shape of the unit cell.

is a highly asymmetric hysteresis, dominated by complete $90°$ switching, and thus showing a large strain change of magnitude 1.09%.

The same concept can be applied to the vortex domain pattern "5346" shown in figure 5.6(a). There are also two types of domain walls in the unit cell, each with area $\sqrt{2}L^2$, corresponding to the two degrees of freedom, a_1 and a_2. Now apply the condition shown in equation (5.9) to examine if the domain walls controlled by a_2 in pattern "5346" are mobile or sessile. As with the case for "5354", the left hand side of equation (5.9) becomes $a_1(1-a_1)\|\mathbf{n}_2 \times \mathbf{n}_3\|$, where $\mathbf{n}_2 = \mathbf{n}_3 = [0,1,1]$. Consequently, this always equals zero regardless the value of a_1. It can also be seen in figure 5.6(b) and (c), that both types of movement of a_1 and a_2 domain walls do not distort the unit cell. Thus both degrees of freedom are always mobile. The velocities of the domain walls are in the form of $v_{(1)} = \dot{a_1}\sqrt{2}L/2$ and $v_{(2)} = \dot{a_2}\sqrt{2}L/2$. A suitable rate potential Ψ_{5346} for linear kinetics is given by

$$\Psi_{5346} = \frac{\sqrt{2}L^4}{4m}(\dot{a_1}^2 + \dot{a_2}^2) \tag{5.21}$$

Again, the loading case of electric field $E_3(t) = E_0\sin(2\pi t)$ at amplitude $E_0 = 1\mathrm{MVm}^{-1}$, along with the stress loading $\sigma_3 = -1.78$ MPa is considered. An initial state of domain pattern "5346" is defined by setting $a_1 = a_2 = 1/2$. This gives a polarization-free state with equal

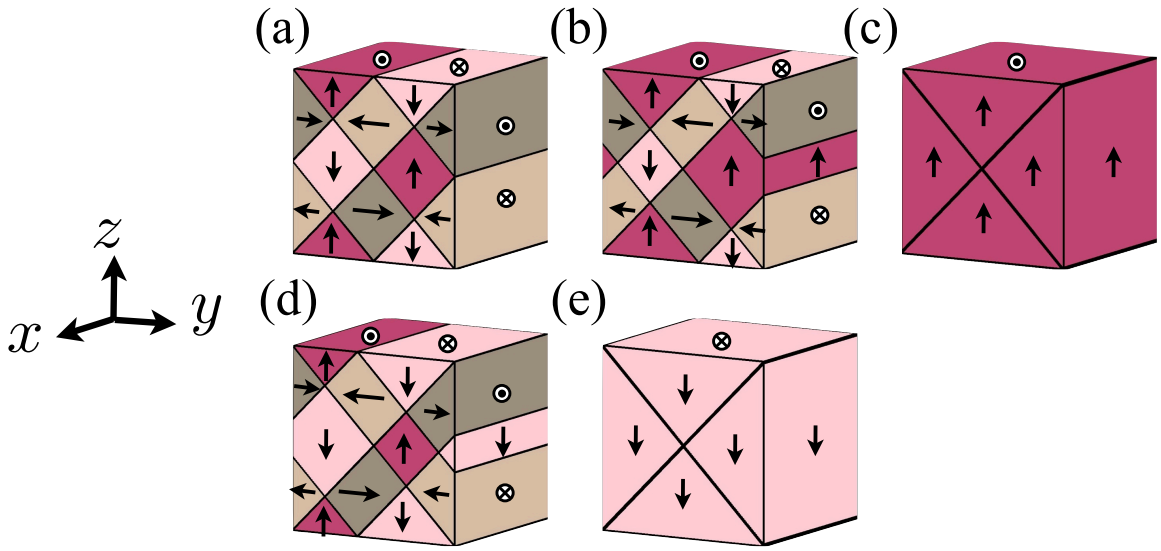

Figure 5.7: The schematic domain evolution for pattern "5346" in the electric loading cycle under stress $\sigma_3 = -1.78\text{MPa}$. (a) The initial state, the stress cannot induce any domain wall movement. (b) $E_3 > 0$, increasing the volume fraction of crystal variant 5. (c) Single domain state "5". (d) When $E_3 < 0$, the volume fraction of crystal variant 6 increases. (e) Single domain state "6".

volume fractions of all four domain types.

Figure 5.4(b) shows a dielectric loop and a symmetric strain hysteresis loop for domain pattern "5346"; the domain evolution is shown in figure 5.7. It is interesting to note that the microstructural state, specified by $a_1(t)$ and $a_2(t)$, evolves along a path such that: a_1 remains equal to a_2 throughout the simulation. This arises because of the symmetry of the applied loading and the initial state, as shown in figure 5.7(a). The applied compressive stress favours crystal variants 3 and 4. However, in this domain arrangement the only way to increase the regions containing variant 3 is to shrink the regions containing variant 4, and vice versa. Thus, the driving force due to the stress does not induce any domain wall movement. When electric field $E_3 > 0$ is applied, variant 5 becomes energetically favoured while variant 6 is energetically unfavourable. Then the domain pattern becomes a single domain state with variant 5 only (figure 5.7(a)→(c)). When $E_3 < 0$, domain walls follow the same evolution path maintaining $a_1(t) = a_2(t)$ and the pattern then reaches another single domain state with variant 6 (figure 5.7(d)→(e)). This complete 180° domain switching results in a dielectric hysteresis loop which has saturated val-